



## Bachelor of Science Thesis

Joint Degree Course in Geosciences  
Ludwig-Maximilians-Universität München  
and  
Technische Universität München

# Mechanisms of intraplate earthquakes: The 2017 Botswana event

Chair of Geophysics  
Department of earth and environmental sciences  
Ludwig-Maximilians-Universität München  
Theresienstraße 41  
80333 München

written by: Thomas Obermaier  
matriculation number: 11747566  
date: 14.08.2020  
supervised by: Dr. Alice-Agnes Gabriel  
Dr. Max Moorkamp  
Dr. Thomas Ulrich



## Abstract

Most seismic activity on earth occurs at plate boundaries. Stable continental regions apart from tectonic stress sources therefore are not known for big events. However, there are some moderate to large intraplate events within stable continental regions and due to their location within plates, they can cause threat to infrastructure and humans in lively areas. The source of stress and which mechanisms enable intraplate earthquakes are still discussed in earth sciences.

Based on an estimated fault trace from resistivity data we studied initial fault stress and relative apparent fault strength to constrain regional stress conditions that enabled the 2017 Botswana intraplate event. We focused on four key parameters: the direction of  $SH_{max}$ , fluid pressure, initial relative fault prestress ratio  $R_0$  and the stress shape ratio. Static analysis results show a strong impact of  $SH_{max}$  directions on local stress conditions and suggest  $SH_{max}$  values from  $132^\circ$  to  $142^\circ$  to be most realistically.

On the basis of the findings from static stress analysis, we set up a dynamic rupture model to specify parameters describing the event properly. Here, we built a mesh which discretizes our model domain in three dimensions and translated a 3D velocity model into 3D material properties, which were assigned to our model domain. Since we simulate dynamic scenarios, we implemented a rapid weakening friction law into our model. We tested our results by comparing our outputs to results published in literature. We found that our model setup for the lithostatic case shows good consistence with the observed results from various authors. However, the simulation under hydrostatic conditions produces a much too large earthquake which maybe is a sign for the state of pressure during the Mojabana earthquake.

[what is rapid weakening friction law?](#)

[simulation under hydrostatic conditions produce too large earthquake](#)

# Contents

<b>Abstract</b>	<b>3</b>
<b>1 Introduction</b>	<b>5</b>
<b>2 Tectonic setting, earthquake characteristics and trigger hypothesis</b>	<b>8</b>
2.1 Tectonic setting and geological history of Botswana . . . . .	8
2.2 The 2017 Botswana earthquake - a summary . . . . .	10
2.3 What caused the 2017 Botswana event? . . . . .	11
<b>3 Static analysis</b>	<b>15</b>
3.1 Modeling the fault geometry . . . . .	15
3.2 Calculation of the R ratio . . . . .	18
3.2.1 Relative fault prestress ratio . . . . .	19
3.2.2 Azimuth of maximum horizontal compressive stress . . . . .	20
3.2.3 Fluid pressure ratio . . . . .	20
3.2.4 Stress shape ratio . . . . .	21
3.3 Results and discussion . . . . .	21
<b>4 Dynamic rupture modeling</b>	<b>25</b>
4.1 Mesh generation . . . . .	25
4.1.1 Mesh dimensions . . . . .	25
4.1.2 Resulting mesh and quality assessment . . . . .	26
4.2 Dynamic rupture modeling setup . . . . .	27
4.2.1 Input files . . . . .	27
4.2.2 Rapid weakening friction law . . . . .	28
4.3 Results and discussion . . . . .	29
4.3.1 Free surface ouput . . . . .	30
4.3.2 Fault output . . . . .	33
<b>5 Conclusion and outlook</b>	<b>37</b>
<b>Bibliography</b>	<b>39</b>
<b>Acknowledgement</b>	<b>44</b>
<b>Statement of authorship</b>	<b>45</b>

# 1 Introduction

The vast majority of seismic activity occurs at plate boundaries. However, there are some large magnitude events within plate interiors as well, where tectonic loading is insignificant (see figure 1). Earthquakes in stable continental regions are spread all over the world. The four  $M \geq 7.0$  New Madrid earthquakes in Central U.S. in 1811 and 1812 [Hough et al., 2000], the Tennant Creek sequence  $M6.3, 6.4$  and  $6.7$  events in central Australia in 1988 [Bowman, 1992] or the 1969  $M6.3$  Ceres earthquake in South Africa [Krueger and Scherbaum, 2014] are some popular examples. Only a few large earthquakes (magnitude 6 and higher) are recorded in history, but due to low attenuation of seismic energy within plate interiors they can cause significant seismic hazard for population and infrastructure, even in well developed regions [Calais et al., 2016].

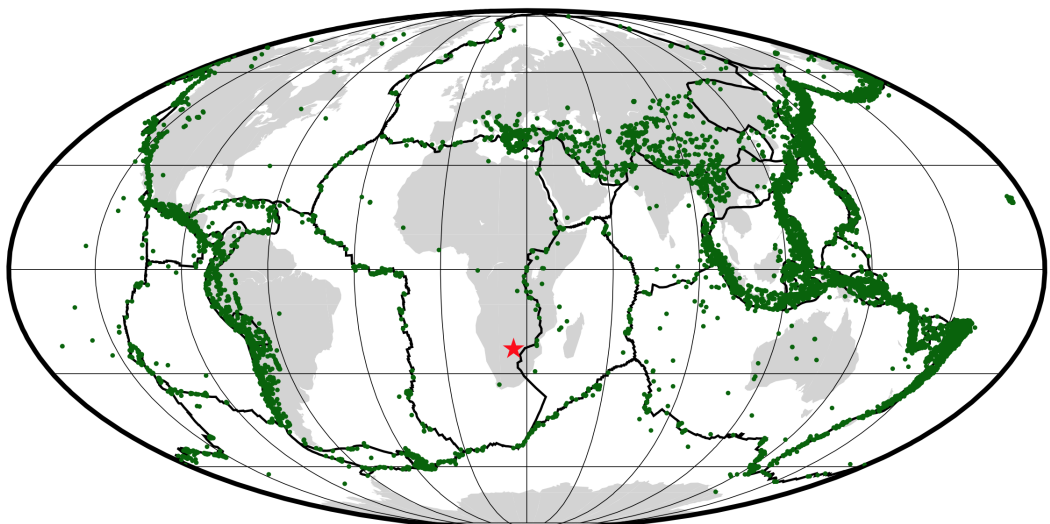


Figure 1: Seismic activity worldwide. Green circles mark events with magnitude  $M>6$  from 1900 up to now (<http://earthquake.usgs.gov/>). The red star shows the location of the 2017 Botswana event. Black lines indicate plate boundaries.

Today, earthquake processes are generally described by stress accumulation (over long time scales) due to motion of tectonic plates at plate boundaries. If a critical stress level is reached and frictional strength is exceeded, an earthquake ruptures and stress is released to the lithosphere. Depending on the strength of the fault and as a result of ongoing stress loading, this can be repeated cyclically and the fault may, regularly or irregularly, rupture again [Kanamori and Brodsky, 2004].

There have been debates in literature about the mechanisms of rupture processes of large intraplate earthquakes all along [P. Talwani, 1988; L. Liu and M. Zoback, 1997; Pollitz et al., 2001; Calais et al., 2016]. Due to the lack of suitable models, concepts for earthquakes at plate boundaries often were applied to intraplate events. As this is the basis for probabilistic earthquake calculation, this view does not appear to be sufficiently justified, with possibly far-reaching consequences. This shows that mechanisms which enable earthquakes in stable continental regions are still poorly understood and further research is required for future engineering design and to improve calculating seismic hazard in well developed and populated regions [M. Liu and Stein, 2016].

The first idea on describing intraplate seismicity was proposed by Sykes [1978], who described the global pattern of intraplate events based on the hypothesis, that these stresses are transmitted over large distances by a rigid and strong continental lithosphere [L. Sykes and Sbar, 1973]. In the following, it was recognized that intraplate seismicity predominantly occurs in old rift structures and along craton boundaries [Mooney et al., 2012]. Talwani [1988, 2017] combined some of the earlier models, which link intraplate earthquakes to stress accumulation on discrete structures in the upper and lower crust to a unified framework for studying intraplate earthquakes. According to Talwani, far field regional stress associated with plate tectonic forces leads to local stress build-up on so called "local stress concentrators" (LSC). These geologic features include shallow plutons, rift pillows, fault intersections or kinks. He distinguished between different sources of stress (following M. L. Zoback, 1992). There are first order mid plate stress fields due to plate tectonic forces, which result in a uniform compressional stress regime over continental regions. And in addition to that, there are second order stress fields associated with specific geologic and tectonic features, the LSC. Locally, the superposition of both can lead to a rotation of the regional stress field with wave lengths of tens to hundreds of kilometers. Stress on LSC accumulates over time and if magnitudes of local stress and regional stress fields are comparable, seismicity occurs. This means, that far field stresses enable intraplate earthquakes, but style and timing of intraplate earthquakes at LSC can also depend on second order stress fields associated with erosion, glacial isostatic adjustment, thermal anomalies and as well, fluids. Thrust faulting, strike slip faulting and horizontal contraction are the main source mechanisms regarding intraplate earthquakes [McNamara et al., 2015] and after Moorkamp et al. [2019], the model of Talwani matches with these source mechanisms. Compatible with the model of Talwani, Moorkamp et al. [2019] proposed, that intraplate earthquakes typically occur on unknown faults and most seismic activity in stable continental regions (SCR) results from far-field stresses due to plate boundary stress build-up.

In 2016, Calais et al. introduced a new model, that challenges the view that intraplate earthquakes occur when local tectonic stress at active faults reaches failure threshold. In that case, large intraplate earthquakes should repeat on the same fault (with very long recurrence intervals), as events at plate boundaries do and the strain rate field should be observable throughout. However, unique measurements of strain accumulation on active geologic structures are still difficult. Further, there is proof, that the locations of large earthquakes between fault systems vary over time [M. Liu, Stein, and Wang, 2011] and after Clark et al. [2012], SCR faults are better characterized by long periods of seismic inactivity intercepted by short periods of concentrated activity. These short time intervals require even shorter strength and stress variations. Therefore, events in

stable continental regions show different spatial and temporal patterns compared to events at plate boundaries [Calais et al., 2016].

Calais et al. [2016] propose, that stable continental region earthquakes are better explained by temporal disturbances of local stress and/or fault strength, which causes release of elastic energy built up and stored in the lithosphere over large time scales, because the observed strain accumulation in most stable continental regions is not fast enough to result in large earthquakes. Therefore, these events do not necessarily happen in regions with seismic history or visible expression of strain accumulation, as the source of strain is given by external and amongst others, nontectonic forces. As a result, they do not need to repeat on observable time scales, what makes concepts of recurrence intervals or fault slip rate unapplicable. In summary, they state that "SCR seismicity is predominantly a transient feature triggered or inhibited by secondary, nontectonic sources of stress change rather than a steady state response of faults to constant tectonic loading" [Calais et al., 2016].

Intraplate seismicity in southern Africa and in particular in Botswana can be described by a small number of moderate to large earthquakes per hundred years and some local clustered present-day seismicity [Wright et al., 2003]. Even if large earthquakes in Botswana are quite rare, in October 1952 a  $M6.7$  event was observed [Hutchins and Department, 1976]. The East African Rift System (EARS) is one of the major seismic hotspots all over the world and accounts for the majority of all seismic events in southern Africa. The Okavango Rift Zone (ORZ) is considered as one of the seismic hotspots in the southern part of the african continent as well. Both, the EARS and the ORZ represent the main sources for seismic activity in this region [Midzi et al., 2018].

The  $M6.5$  3rd April 2017 Botswana earthquake and its aftershocks are located in a region with no previously known large earthquakes and little to unsignificant tectonic activity [Moorkamp et al., 2019]. These events occurred in the orogenic Protoerozoic Limpopo Belt between Archean Kaapvaal and Zimbabwe cratons and close to the junction of Limpopo Belt and Kaapvaal cratonic region [Materna et al., 2019] (see figure 2). The so-called Moijabana event is characterized by a hypocentral depth in the range of  $20 - 29\text{ km}$  [cf. Kolawole et al., 2017; Gardonio et al., 2018] with a NW-SE striking and NE-SW dipping normal fault plane [Kolawole et al., 2017]. It is the largest event within stable continental regions since the 1988 Tennant creek earthquakes.

There is an ongoing debate on how the 2017 Moijabana event was triggered. It has been proposed, that the earthquake occurred in an ancient zone of weakness, corresponding to stress exerted by the EARS [Materna et al., 2019]. Gardonio et al. [2018] consider a temporarily pulse of fluids as trigger mechanism most likely. Another proposal was made by Fadel et al. [2020], wherein they similarly suggest fluids or melt as an explanation for nucleating the earthquake, but they link the source of these fluids to the EARS. Gas extraction in the area of the earthquake [Barbee, 2017] lead to the question, whether anthropogenic activities triggered the event. This was refuted and is not considered as a possible explanation anymore [Albano et al., 2017].

In this thesis, we perform static stress analysis to constrain regional stress conditions in the epicentral region and several dynamic rupture simulations based on a 3D shear wave velocity model in order to provide insights on what could have triggered the 2017 Botswana earthquake.

## 2 Tectonic setting, earthquake characteristics and trigger hypothesis

### 2.1 Tectonic setting and geological history of Botswana

According to Moorkamp et al. [2019], boundaries of local tectonic units of deeper crustal and upper mantle structures in Botswana are not fully explored up to now [cf. Khoza et al., 2013; Leseane et al., 2015; Yu, K. H. Liu, et al., 2015; Pastier et al., 2017, Fadel, Meijde, et al., 2018]. Fadel et al. [2018] argue, that poor coverage of southern Africa with seismic stations results in low resolution of crustal and upper mantle structures and there is little information about geodynamics as well. Nevertheless, a careful view on local tectonics is essential for understanding Botswanas seismic activity.

In general, geology in Africa can be macroscopically described by Archean cratons with Protoerozoic mobile fold belts in between [Fadel, Paulssen, et al., 2020]. Especially Botswana mainly consists of the Congo Craton in the northwest and the Kalahari Craton in the south and east [Fadel, Meijde, et al., 2018]. The latter was created due to the collision of Archean Kaapvaal and Zimbabwe Cratons with the crustal Limpopo Belt block in between in the late Paleozoic and is characterized by low-grade metamorphic rocks [Begg et al., 2009]. After Priestley et al. [2006], the Kalahari Craton was not reworked during the last 2.3 *Ga* (neglecting intrusions and orogenesis within the craton). The Limpopo Belt (often referred to as Limpopo-Shashe orogenic belt) was reworked several times in Paleoprotoerozoic and now consists of granite-greenstone and granulite terraines [Adams and Nyblade, 2011].

In Paleoprotoerozoic, Magondi, Okwa and Kheis Belts and the Rehoboth Province were built west and north to Kalahari Craton [Jacobs et al., 2008; Schijndel et al., 2014]. The Magondi (also referred to as Makondi) Belt is often considered as the southwestern terminus of the EARS [Modisi et al., 2000; Bufford et al., 2012] and is most likely described by a network of smaller Quaternary rift basins [Midzi et al., 2018]. Today, this area is covered by a thick Phanoerozoic sediment layer [Pretorius, 1984]. The Kheis-Okwa-Magondi Belt is bounded to the Paleoprotoerozoic Kalahari Suture Zone (KSZ). The Archean geological units (Kalahari Craton, Zimbabwe Craton, Limpopo and Kheis-Okwa-Magondi Belts) are seperated from the Protoerozoic units (Damara and Ghanzi-Chobe Belts, Rehoboth Province) through the KSZ [Reeves, 1978].

The Damara Belt and Ghanzi-Chobe zone in the northern part of Botswana grew during Neoproterozoic collision of the Kalahari and Congo Cratons [Khoza et al., 2013; and references therein]. The Okavango Rift Zone cuts through both areas and is located in the northern part of Botswana [Fadel, Meijde, et al., 2018; figure 1]. There are two areas called Nosop and Passarge Basin that cover Rehoboth Province and flanking regions with a thick sediment layer (10 km and more) [Pretorius, 1984]. Therefore, the structure of this regions is not explored in detail.

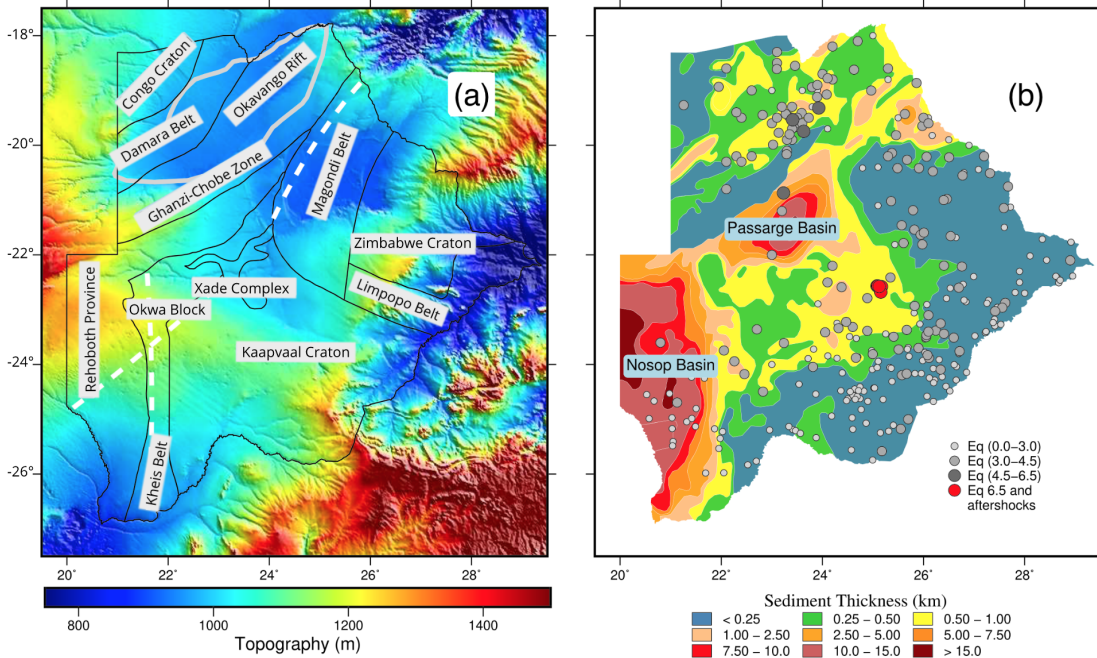


Figure 2: Modified figures from Fadel, Paulssen, et al., 2020 (Figure 1(c) and 1(d)) with location of KSZ from Fadel, Meijde, et al., 2018, figure 1).

- (a) Topographic map of tectonic units in Botswana. The dashed, white lines indicate the Kalahari Suture Zone.
- (b) Sedimentary thickness map and earthquake distribution. Red circles show 2017 Botswana event and its aftershocks.

Tectonic activity in southern Africa is mostly controlled by the EARS. This rifting system describes the extension between the Somalian plate and the African plate (Nubian plate) with an extension from 4 – 6 mm/year in the north to 1 – 2 mm/year in the south (see figure 3) [Demets et al., 2010]. Here, the rift is divided into the eastern and western continuations [Kinabo et al., 2007]. The southwestern branch causes slow extension in Botswana and there is a debate whether the EARS extends up to the Okavango Rift Zone [Leseane et al., 2015; Yu, K. H. Liu, et al., 2015; Yu, Gao, et al., 2015].

## 2.2 The 2017 Botswana earthquake - a summary

In the following, a short summary of the 2017 Botswana earthquake is given.

The  $M6.5$  normal slip earthquake on April 3rd in Moijabana, Botswana was located within the Paleoproterozoic Limpopo Belt, close to the junction to Archean Kaapvaal cratonic region and more than  $100\ km$  west of Moijabana. This area is considered as a seismically quiet province [Kolawole et al., 2017]. Some authors place the earthquake within Magondi Belt [cf. Albano et al., 2017; Fadel, Paulssen, et al., 2020], whereas Gardonio et al. [2018] rather places it within the Kaapvaal Craton, close to the border of Magondi and Limpopo Belt. As already discussed in the chapter before, junctions and borders of geologic units are not fully explored. Following Kolawole et al. [2017], Materna et al. [2019] and Moorkamp et al. [2019] we assume the Limpopo Belt to be the geologic unit where the earthquake happened for this thesis, since there is no significant impact on our model, whether it is Magondi or Limpopo Belt. It is suggested that the earthquake occurred along an ancient thrust/reverse fault that was reactivated and turned into a normal fault [Kolawole et al., 2017; Moorkamp et al., 2019]. Interestingly, Moorkamp et al. [2019] found that the Botswana event, with its normal faulting mechanism and extensional behaviour, is not compatible with the model of Talwani (see chapter 1, Introduction). However, normal faulting is consistent with stress conditions (large scale extension) of southern Africa after Stamps et al. [2010].

Shaking effects due to the earthquake were felt throughout southern Africa. Damage was not extensive because of the distance of the earthquake location to vibrant areas. According to the thick sand coverage of the epicentral region, no visible expression of the earthquake is left [Midzi et al., 2018].

The depth of the earthquake is placed in the mid to lower crust in a range of 20 to  $29\ km$ . Here, most authors consider depths greater than  $25\ km$  as most suitable and therefore characterize this earthquake as a deep crustal event.

Most authors agree on a magnitude of  $M6.5$  like suggested by USGS W-phase moment tensor. Except Materna et al. [2019], who consider  $M6.4$  more likely due to higher shear modulus at lower depths. However, differences in this order of magnitude are negligible for this project.

Albano et al. [2017] suggests a mean slip of  $2.7\ m$ , whereas Materna et al. [2019] uses a slip of  $0.66\ m$  to describe the source. These differences probably are the result of using different fault dimensions. Materna et al. [2019] uses a slip patch 4 times bigger than Albano et al. [2017] does to describe the source, and as the magnitude of an earthquake is proportional to the size of the fault plane and the displacement, these values match each other. The findings of Kolawole et al. [2017], suggesting a slip of  $1.8\ m$  and a different fault dimension, can be interpreted in the same way. Due to the fact that Materna et al. [2019] uses combined InSAR and teleseismic observations and Kolawole et al. [2017] uses aeromagnetic and gravity data integrated with DInSAR, these findings may be more reliable than models from InSAR data alone, carried out by Albano et al. [2017]. Therefore the slip of the 2017 Moijabana event is most likely smaller than  $2\ m$ .

Both Albano et al. [2017] and Kolawole et al. [2017] suggest a NW striking and NE dipping fault with a dipping angle of  $65^\circ$  and  $72^\circ - 74^\circ$ , respectively. The large dipping angle of the fault is consistent with a deep source of the main event and the closeness

of the fault to the epicentral area of approximately 7 km southwest to the mainshock [Kolawole et al., 2017]. Similar to that, Gardonio et al. [2018] and Materna et al. [2019] found a NW striking and NE dipping fault solution. However, they claim that there is a second possible fault orientation that matches their observations. Derived from InSAR and teleseismic observations, Materna et al. [2019] consider a SE striking ( $126^\circ$ ) and SW dipping fault to be the most suitable solution. Gardonio et al. [2018] found a similar solution to that, but their dipping angles differ up to  $30^\circ$  to the findings of Materna et al. [2019]. Here, differences may be explained by different modeling strategies [Materna et al., 2019]. In chapter 3.1 we use a NW-SE striking and NE dipping fault to model our geometry, as this better represent the aftershock locations. The direction of the fault motion is described by the rake angle, which is per definition  $-90^\circ$  for normal faulting events [Shearer, 2009]. Albano et al. [2017] found a rake angle of  $-131^\circ$ . Here, Materna et al. [2019] suggest a smaller rake angle of  $70^\circ - 107^\circ$ , which better suits normal faulting.

The Mojabana event was part of a sequence of 15 events with  $M \geq 5$  in a period of 4 months after the main shock [Moorkamp et al., 2019]. Investigations on aftershock distribution were conducted by the Council for Geoscience (CGI) and the Botswana Geoscience Institute (BGI), who analyzed the data of more than 500  $M \geq 0.8$  aftershock events. They found two obvious clusters. The first aftershocks occurred in the northern cluster, whereas most of the later events occurred in the southern cluster. This suggests that a NW-SE oriented splitted fault plane is the source of the aftershock events. In this case, orientations of mainshock and aftershock fault planes coincide [Midzi et al., 2018].

The debate on what triggered the earthquake is still topic in literature. Possible mechanisms and approaches pursued so far are discussed in the next chapter.

## 2.3 What caused the 2017 Botswana event?

Possible models and trigger mechanisms for earthquakes in stable continental regions were introduced in chapter 1, Introduction [cf. P. Talwani, 1988; L. Liu and M. Zoback, 1997; Pollitz et al., 2001; Calais et al., 2016]. In the case of the 2017 Mojabana, Botswana event, different approaches were pursued so far. A short overview is given in this chapter.

After the theory of anthropogenic influence on triggering the Mojabana event was refuted due to a qualitative evaluation, whether induced Coal-Bed-Methane (CBM) extractions can produce stress perturbations required to trigger large events by Albano et al. [2017], there are two possible explanations for nucleating the earthquake left to discuss.

The idea that fluids triggered the 2017 Botswana event was proposed by Gardonio et al. [2018]. They consider a transient pulse of fluids from a deep source as trigger mechanism in a close to failure loaded fault network as most likely. They claim that the earthquake did not require previously localized stress or strain accumulation, which

means that far field and local stress accumulation did not contribute to nucleate the earthquake. In evidence for the fluid migration hypothesis Gardonio et al. [2018] raise the following arguments: The event occurred in the lower crust, what is often considered as evidence for a mafic composition [Craig et al., 2011]. However, their seismic surveys show a Poisson ratio of 0.25 and a crustal density of  $2860 \text{ kg/m}^3$  for the Kaapvaal Craton, what is typical for felsic composition [James et al., 2003]. Gardonio et al. [2018] argue, that in this depth and under hydrostatic pore pressure, felsic crust does normally not flow without differential stress and therefore pore fluid pressure had to be different to hydrostatic conditions to activate brittle failure. The two observed series of swarm-like foreshocks may be indicative for a pulse of high pore fluid pressure, too. The source of the fluids is said to be in the upper mantle, where great amounts of fluids are stored underneath Africa [Leseane et al., 2015]. As a consequence Gardonio et al. [2018] suggest, that the crust in stable continental regions stores elastic stress over long time scales. After triggered, the crust can release stored stress in a series of events.

Further evidence for the fluid trigger hypothesis may be an observed magnetic-low signature for the Moijabana fault by Kolawole et al. [2017]. According to the findings from Mosley [2010], the fault could serve as conduit for fluids within the crust, while magnetic lows can result from weathering processes, where iron dissolves due to fluid alteration [Kolawole et al., 2017].

Moorkamp et al. [2019] challenged the view that fluids triggered the earthquake due to surface wave and magnetotelluric data observations. Although the observed crustal structures allow fluid release from the upper mantle to trigger the earthquake, like suggested by Gardonio et al. [2018], depths of conductivity structures indicating fluids do not coincide with the hypocentral depth. Furthermore, a homogeneous resistivity distribution in upper mantle is most likely a sign of homogeneous hydrogeological conditions. According to that, fluid triggering would require a spatially restricted source region or an ambient water resource within the mantle and can therefore not be excluded in general. Consequently, they can not distinguish whether fluids or a different trigger mechanism is responsible for nucleating the earthquake.

But what Moorkamp et al. [2019] propose is that the recent events are controlled by the interplay of a weak upper mantle and weak crustal structures, kind of like Materna et al. [2019] did. Here, the weak zone in the upper mantle results from reduced grain sizes, which is a sign for reduced viscosity, but restricted in depth and therefore no sign for mantle upwelling. As the source of stress to reactivate ancient faults in this region they exclude the ORZ, because this does not fit with the required orientation of tensional stress. Though, the focal mechanism matches with local stress conditions and therefore far-field stress and tectonic loading may have played a role in local stress accumulation.

The results from Rayleigh wave group and phase velocity observations conducted by Fadel et al. [2020], lead to the second possible trigger mechanism for the 2017 Botswana earthquake: a connection to the EARS.

Low velocity anomalies within the crust can serve as conduits for hot fluids from the mantle and for example trigger earthquakes at the Okavango Rift Zone [Leseane et al., 2015]. Fadel et al. [2020] link the southwestern continuation of the EARS to the ORZ and to the region of the 2017 Botswana earthquake by imaging a low upper mantle

shear wave velocity zone from the EARS to the epicentral location [Fadel, Paulssen, et al., 2020; figure 4B-B']. This leads to the hypothesis, that fluids or melt, migrated from the upper mantle of the EARS southward extension, triggered brittle failure of the Botswana event. They consider this possibility most likely, because the observed low-velocity zone of 3%, which extends over a narrow zone of smaller than 30 km, can hardly be explained by temperature or compositional variations.

After that, the proposed fluid trigger mechanism proposed by Gardionio et al. [2018] would more likely be linked to the EARS.

Another proposal featuring the EARS hypothesis was made by Materna et al. [2019], who consider the southward-propagating EARS as the source of stress, that forced an ancient zone of weakness between two cratonic blocks to fail, due to contrasts in stress or material properties within that weak zone. They found that the earthquake lasted about 10 s, but with two distinct sections. Different rise times, compared the two sections, are taken as an indicator for contrasts in stress values or material properties. Altough Materna et al. [2019] did not commit on the cause of the earthquake, they proposed that non-tectonic stress or strength disturbances may lead to failure.

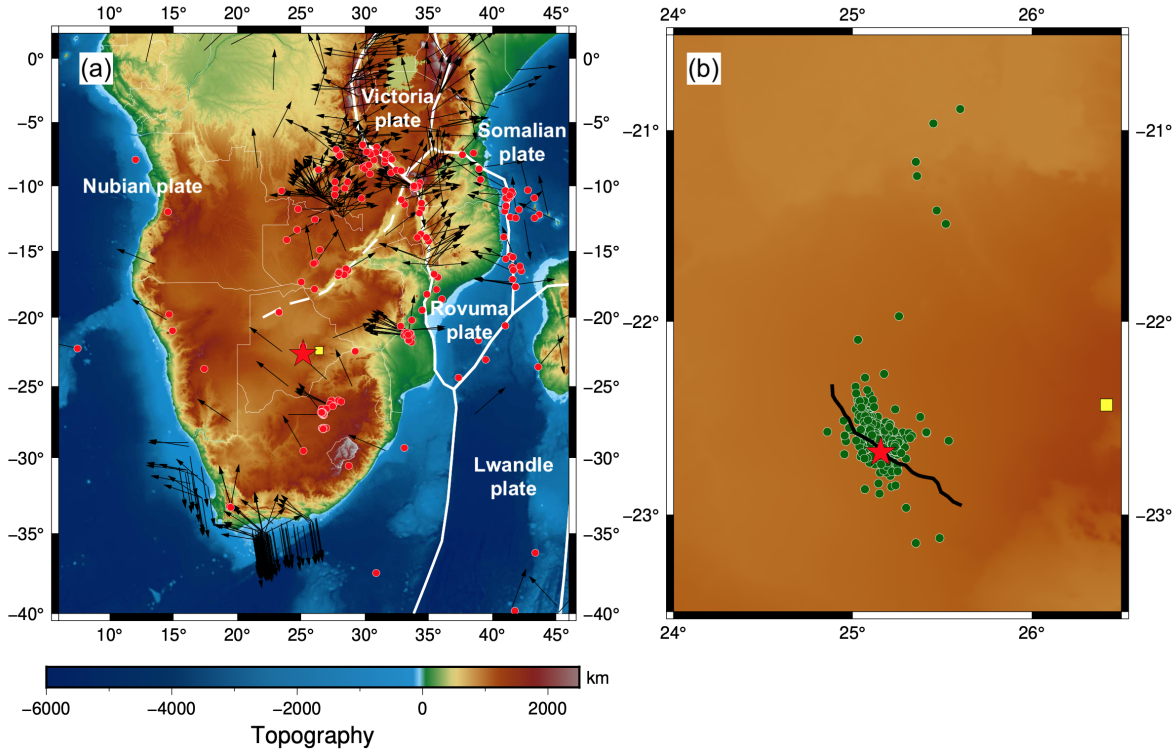


Figure 3: (a) Topographic map of southern Africa. Thin white lines indicate borders, thick white lines plate boundaries. The dashed white line shows the suspected Okavango Rift location. SHmax directions from World Stress Map 2016 are represented by black arrows [Heidbach et al., 2016]. Red circles show earthquakes from 1900 up to now with  $M > 5$  (<http://earthquake.usgs.gov/>), where the red star locates the 2017 Botswana event. The location of the city Mojabana is marked by a yellow square.  
 (b) Zoom into figure (a). Aftershock locations are represented by green dots. The black line indicates the fault corresponding to the 2017 Botswana earthquake.

# 3 Static analysis

Following the method of Ulrich et al. [2019a], we studied initial fault stress and relative apparent fault strength based on seismo-tectonic observations, fluid pressurization and the Mohr-Coulomb theory of frictional failure. This method was developed to better quantify frictions on and strength of natural faults, which often is very difficult and simplifies the parametrization of our static analysis model. Only four parameters have to be examined to fully describe the state of stress and relative strength properties of the fault system, if the state of stress is Andersonian (one principal stress axis needs to be vertical): the initial relative prestress ratio  $R_0$ , the stress shape ratio  $\nu$ , the azimuth of maximum compressive stress  $SHmax$  and the fluid pressure ratio  $\gamma$  [Palgunadi et al., 2020].

Based on static analysis, where stress and strength properties are pre-constrained and therefore non-uniqueness of the dynamic models is reduced, only a few simulations are required to adopt the best fitting dynamic rupture model. Costly supercomputing resources can be saved by avoiding a trial-and-error approach.

Optimal stress parameters can be extracted from static analysis results. This stress configuration maximizes the  $R$  ratio across the fault and the shear orientation needs to be consistent with observed ground deformations and the focal mechanism of the earthquake. Then, dynamic rupture simulation can be used for further investigation.

## 3.1 Modeling the fault geometry

Based on a data set from Max Moorkamp that provides the fault trace of the 2017 Botswana event in cartesian coordinates (UTM), we use a simple python script from Thomas Ulrich to model the fault in depth. The fault location according to the fault trace was estimated from the resistivity distribution in shallow depths (see figure 4). Uncertainties in the exact location and shape can not be excluded. There is no need to use spherical coordinates (latitude, longitude), as the area of interest is small compared to earth's curvature.

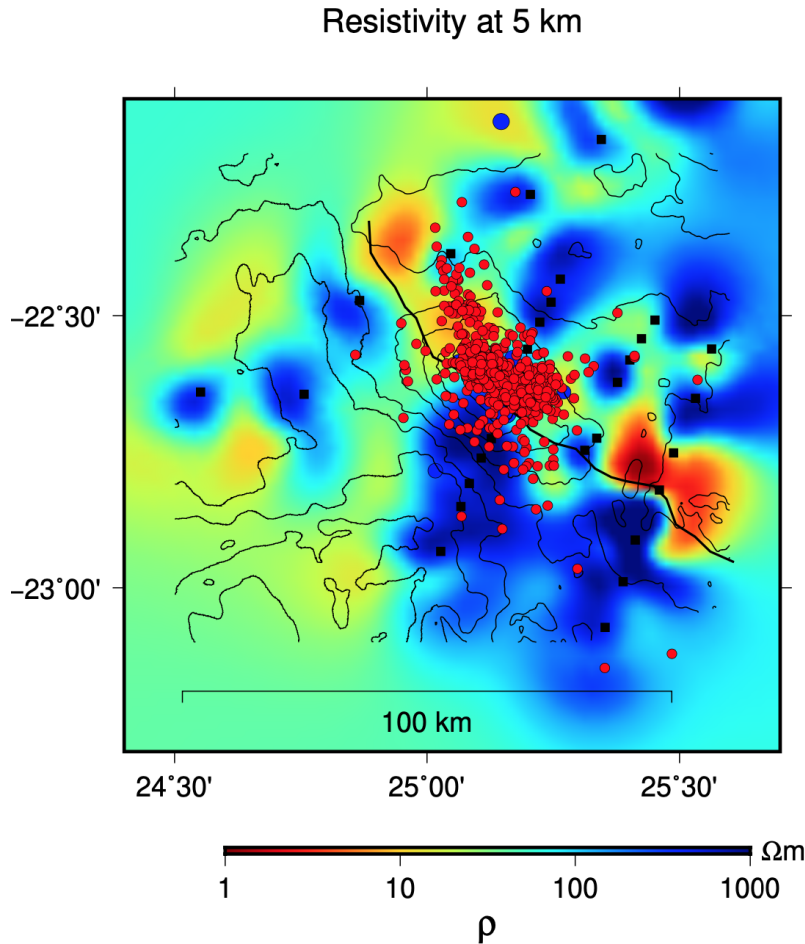


Figure 4: Resistivity model from Max Moorkamp with estimated fault trace (black line). Red dots indicate the aftershock distribution.

To avoid trouble with dynamic rupture modeling due to unplanarity of the fault, the fault trace is smoothed by using a characteristic length. The number of data points to be fitted is determined by the ratio between smoothing parameter and length of the fault. We use a smoothing parameter of  $10^7$  and the length of the fault trace is  $108.46\text{ km}$ , which leads to a characteristic length of about  $92\text{ m}$ . This means, that for the interpolated fault shape, grid points are set to be in a distance smaller than  $100\text{ m}$ . Considering, that the horizontal length of cells used in the model of Moorkamp et al. [2019] is  $2\text{ km}$ , the characteristic length of about  $92\text{ m}$  is detailed far enough, but does not represent a real accuracy of the real fault trace in this scale. In the first step, a constant dip angle of  $73^\circ$  NE is assumed (cf. Gardonio et al., 2018 and Kolawole et al., 2017). A listric fault can be generated by using a depth-dependent dip angle. The fault of the Mojabana event has no surface expression. Therefore, the modeled fault is placed below the surface, realized through an additional offset in depth of  $5\text{ km}$ . The total depth of the fault is restricted by the end of the seismogenic zone, where ductile deformation is predominant. Here, we estimate the depth of the slip to be  $37\text{ km}$ . These values are derived from the kinematic model of Materna et al. [2019], figure 6 and the location of the aftershocks.

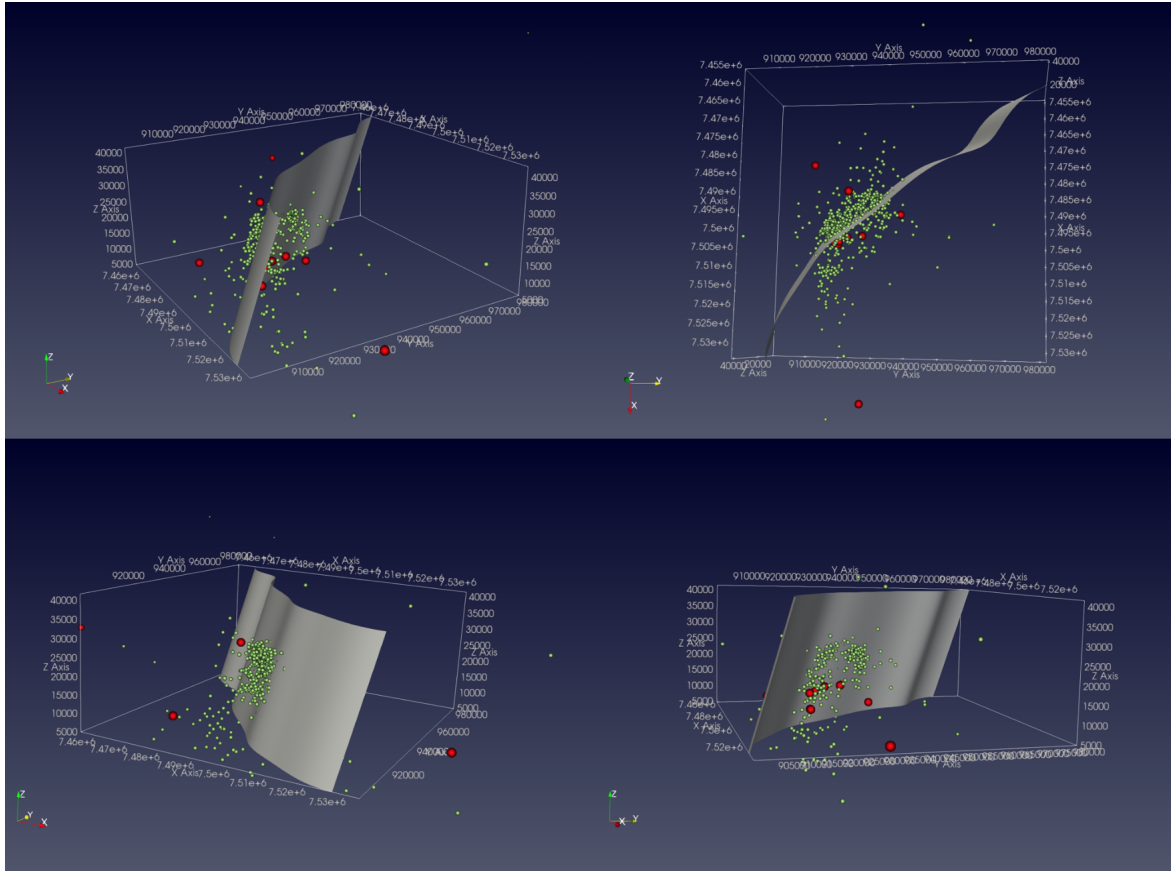


Figure 5: Fault geometry with detailed distribution of the aftershocks (green spheres) and event locations from USGS earthquake catalogue (red spheres). Note, the depth is given in positive values.

## 3.2 Calculation of the R ratio

The target value we take a closer look at, is the relative prestress ratio  $R$ . It describes the spatially distributed fault strength in our model on every point of the fault. In a first step we will only vary the stress parameter  $SHmax$  within its uncertainties and calculate the distribution of the relative prestress ratio  $R$  on the fault plane for each configuration. The initial relative prestress ratio  $R_0$  and the stress shape ratio  $\nu$  are set to a constant value. The fluid pressure  $\gamma$  is kept constant at a hydrostatic level in order to examine, whether fluid pressurization is necessary to describe our failure system.  $R_0$  and  $\gamma$  may be adopted for a better fit of the model to the characteristics of the earthquake.

Besides  $R$ , we use calculations of the rake angle to better constrain our regional stress setup. The rake angle needs to be consistent with the normal faulting earthquake mechanism of the 2017 Botswana event and therefore may exclude some stress constellations.

In the following, some parameters and their corresponding values will be shortly introduced. The most important, and also varied parameters ( $R_0$ ,  $SHmax$ ,  $\gamma$ ,  $\nu$ ) will be explained in detail in the next subchapters.

There are three values describing the frictional behaviour of our model. Using the friction law after Byerlee [1978], which describes strong static rock behaviour, the static friction coefficient  $\mu_s$  is equal to 0.6. The dynamic friction coefficient  $\mu_d$  was experimentally derived by Alice Gabriel's working group to a small value of 0.01 to 0.1. Frictional cohesion  $c$  is set to a small value in order to not neglect normal surface stresses and to include linear depth dependency of stress.

To describe the fault environment lithologically, **rock density  $\rho$**  (in general:  $\rho_{crust} = 2670 \text{ kg/m}^3$ ) and **fluid pressure  $\gamma$**  are combined and result in efficient density  $\rho_{eff}$ .

The stress tensor is not calculated for every depth. Therefore,  $z_{ref}$  defines the characteristic depth for computing the stress tensor, which is later scaled depth-dependently. This parameter can cause large deviations in the results, so this value requires handling with care. We assume the depth of the hypocentre (29 km) as characteristic depth for our model.

**The state of stress is assumed as Andersonian.** Therefore, the vertical principal stress axis  $s_v$  is needed to be defined. Due to the normal faulting 2017 Botswana earthquake, the vertical axis for extension is 1 [Clauser, 2016]. The stress shape ratio  $\nu$  describes the state of stress in terms of magnitude and is explained later in detail.

**The software SeisSol is usually used for dynamic rupture modeling in the workgroup of Alice Gabriel.** This software requires a coordinating vector to be defined as ( $v_x = 0$ ,  $v_y = 0$ ,  $v_z = -1$ ). If this vector is perpendicular to normal of some cells in our modeled fault, it is necessary to add  $v_x$  and  $v_y$  components [Thomas Ulrich, personal communication].

For a detailed overview of all parameter values and variation ranges see table 3.2.1. Basically, from these parameters the script computes the stress tensor and given the fault orientation, it computes the tractions and then the  $R$  ratio over the fault.

Parameter	Value	Variation
$R_0$	0.8	0.7 - 0.9
$SHmax$	142°	± 40°
$\gamma$	0.37	$0.37 < \gamma < 1$
$\mu_s$	0.6	
$\mu_d$	0.1	
$c$	0.1	
$\rho$	2670 kg/m³	
$\rho_{eff} = \rho(1 - \gamma)$	1735.5 kg/m³	< 1735.5 kg/m³
$z_{ref}$	29 km	
$s_v$	1	
$\nu$	0.5	
$v_x$	0.1	
$v_y$	0.1	
$v_z$	1	

Table 3.2.1: Parameter values and variations used for calculating the ratio of R over the modeled fault

### 3.2.1 Relative fault prestress ratio

Unless otherwise stated, the following is mostly based on declarations from Palgunadi et al. [2020], 'Fault strength and loading stresses' and originates from Ulrich et al. [2019a, 2019b].

The **initial relative fault prestress ratio  $R_0$**  describes how close a virtual, optimally oriented fault is to failure (after Mohr-Coulomb theory, Aochi and Madariaga, 2003) and in general, the relative strength of the fault plane. Optimally oriented means, that this fault reaches failure level before differently oriented faults do, considering homogeneous initial stress and stressing rate. Failure is reached when shear to normal stress ratio (Coulomb stress) is maximized and equal to the static friction coefficient  $\mu_s$ . In other words,  $\mu_s$  describes a local strength of the fault. Actually, faults are not oriented optimally in real life. However, only little of the modeled faults need to be at failure equilibrium to trigger dynamic rupture. After nucleating, rupture is spreading over the whole fault and even parts, that have been below failure level, break.

The parameter  $R$  describes the relation between potential stress drop  $\Delta\tau$  to breakdown strength drop  $\Delta\tau_b$  and shows how stresses differ in magnitude. This parameter is a scale for the energy release of an earthquake due to stress drop. Following the definition,  $R$  is always lower or equal to  $R_0$ . Critical loading of an optimal oriented fault is given, if  $R_0 = 1$ . If one point is both on the modeled and the optimal fault, the value for  $R$  at this point is equal to  $R_0$ . The relative prestress ratio  $R$  is given by:

$$R = \frac{\Delta\tau}{\Delta\tau_b} = \frac{\tau_0 - \mu_d\sigma_n}{c + (\mu_s - \mu_d) \times \sigma_n} \quad (3.2.1)$$

where  $\tau_0$  is initial shear traction on the fault plane,  $\sigma_n$  normal traction on the fault

plane,  $c$  frictional cohesion,  $\mu_d$  dynamic friction coefficient and  $\mu_s$  static friction coefficient.

### 3.2.2 Azimuth of maximum horizontal compressive stress

Crustal stress patterns and stress sources can be described by the directions of principal stresses. The World Stress Map (WSM) provides data about the present-day stress field. The typical value to extract from this data is **the azimuth of maximum horizontal compressive stress  $SHmax$** , ranked by quality indicators.

Under Andersonian stress regime,  **$SHmax$  coincides with the horizontal projection of the greatest sub-horizontal stress** [Thomas Ulrich et al., 2019a].  $SHmax$  is the parameter, which will be varied for static analysis primarily. According to bad measurement data for Botswana (quality factor E) we need to vary the values within its uncertainties of  $\pm 40^\circ$  [Heidbach et al., 2016]. The earthquake location of the 2017 Botswana event is  $22.678^\circ\text{S}$ ,  $25.156^\circ\text{E}$  [Kolawole et al., 2017]. The World Stress Map 2016 data set provides 3 measurements located in vicinity to the earthquake.

Location	$SHmax$	Quality factor
$22.5^\circ\text{S}, 23.5^\circ\text{E}$	$143^\circ$	E
$25^\circ\text{S}, 24^\circ\text{E}$	$142^\circ$	E
$21.5^\circ\text{S}, 27.5^\circ\text{E}$	$22^\circ$	E

Table 3.2.2: Measurements for SHmax provided by the World Stress Map [Heidbach et al., 2016]

### 3.2.3 Fluid pressure ratio

Fluid pressure  $P_f$  is given by:

$$P_f = \gamma \sigma_c = \gamma \rho g z \quad (3.2.2)$$

where  $\sigma_c = \rho g z$  is the lithostatic pressure and  $\gamma$  is the fluid pressure ratio. In crustal regions we assume, that fluid pressure is proportional to lithostatic pressure (after Thomas Ulrich et al., 2019a). Hydrostatic pore pressure is given by  $\gamma = 0.37$ . Higher values represent an overpressurized state of stress. If our static analysis model does not coincide with the observed earthquake characteristics, the fluid pressure is a parameter we will vary to meet our requirements (besides  $SHmax$  and  $R_0$ ).

It is to be noted, that **the fluid pressure ratio** and the **effective confining stress** are two different parameters. The effective confining stress is given by:

$$\sigma_{eff} = (1 - \gamma) \sigma_c = (1 - \gamma) \rho g z \quad (3.2.3)$$

### 3.2.4 Stress shape ratio

The stress shape ratio  $\nu$  is a parameter to describe the fault domain. After Palgunadi et al. [2020], the stress shape ratio creates differences between different stress styles. It is indicative, whether we have one dominating principal horizontal stress direction or two principal horizontal stress directions, with nearly the same amplitude. For this purpose, principal stress amplitudes  $s_i$  are balanced by:

$$\nu = \frac{s_2 - s_3}{s_1 - s_3} \quad (3.2.4)$$

Considering normal faulting, extensional regimes like we have for the 2017 Botswana event, where  $s_1$  is vertical,  $\nu = 0.5$  means pure extension,  $\nu < 0.5$  transpression and  $\nu > 0.5$  transtension. To begin with our static analysis, we assume pure extension.

## 3.3 Results and discussion

By proceeding purely static analysis, we want to constrain regional stress conditions. Based on that, we want to restrict the parameter space of all varied parameters  $R_0$ ,  $SHmax$  and  $\gamma$  for dynamic rupture modeling.

Due to extensive uncertainties of  $SHmax$  values, it is obvious to reduce this parameter space first and foremost. Figure 6 shows the result using parameters  $R_0 = 0.8$ ,  $\gamma = 0.37$  and variable  $SHmax$  from  $102^\circ$  to  $182^\circ$ . In general, we see large discrepancies between the individual figures that show the distribution of the  $R$  ratio, especially between those who show the rake angle distribution. This outlines that the azimuth of maximum compressive stress is a striking feature for our stress setup.

The mainshock and the aftershocks are, in horizontal direction, mostly located in the center of the fault (see figure 5). Therefore, we can exclude  $SHmax$  values  $162^\circ$ ,  $172^\circ$  and  $182^\circ$ , as they show small values for the  $R$  ratio in the center of the fault and according to that, only small ability to sustain rupture.

The focal mechanism of the 2017 Botswana event is normal faulting, which requires tractions compatible with this type of earthquake mechanism. The rake angle is used to describe how the hanging wall moves during rupture. Extension therefore requires a negative value of the rake angle, which is per convention  $\pm 180^\circ$ , measured relative to fault strike. Pure extension then is given by a rake angle of  $-90^\circ$  [Shearer, 2009]. The script used to calculate the rake angle on every point of the fault gives angles from  $0^\circ$  to  $360^\circ$ . In this case, extension corresponds to a value of  $270^\circ$ . According to figure 7,  $SHmax$  values smaller than  $112^\circ$  and bigger than  $152^\circ$  are insufficient to generate a rake angle compatible with normal faulting. Together,  $R$  and rake calculations suggest to constrain the parameter space of  $SHmax$  at least to  $112^\circ$  -  $152^\circ$ .

Interestingly, the variation of the fluid pressure  $\gamma$  does not produce significant changes in the distribution of the  $R$  ratio and the rake angle on the fault. Considering the fact that fluids affect the stress drop magnitude, which becomes smaller with increasing fluid pressure and is directly related to  $R$ , we can not say for sure why we do not see differences in our static analysis plots. Therefore, we keep fluid pressure variations for the dynamic rupture modeling approach and do not constrain the parameter space of  $\gamma$ .

Another interesting finding from static analysis came up with the variation of the relative prestress ratio  $R_0$ . Values in the range from 0.7 to 0.9 all produce comparable distributions of the  $R$  ratio over the fault, relative to the absolute scale. However, this might be due to the static modeling approach and will be better seen in dynamic rupture modeling. Therefore, the parameter space of  $R_0$  will not be reduced and still reaches from 0.7 to 0.9 for the dynamic rupture model.

At this point of the thesis we can return to the original question: what drives intraplate seismicity?

Calais et al. [2016] argue, that short-time perturbations of local stress or fault strength in a prestressed lithosphere lead to intraplate earthquakes rather than reaching failure threshold due to accumulated tectonic stress. Static analysis results show that the direction of maximum horizontal stress  $SH_{max}$  plays a main role in forcing a fault to fail, but there is no configuration that shows critical loading of the fault ( $R \approx R_0$ ). The parameter  $SH_{max}$  describes regional stress conditions and the relative prestress ratio  $R$  on our fault (in given orientation) strongly depends on the value of  $SH_{max}$ . Considering that tectonic loading rates are negligible for intraplate earthquakes [Calais et al., 2016] and therefore a trigger mechanism is required to nucleate the earthquake, the model of Calais fits with our observations and it is quite possible, that transient changes of local stress or fault strength in a prestressed lithosphere have enabled the Mojabana intraplate earthquake.

However, since this is only one indication, it is necessary to carry out further investigations to provide more reliable insights to answer the question of intraplate seismicity.

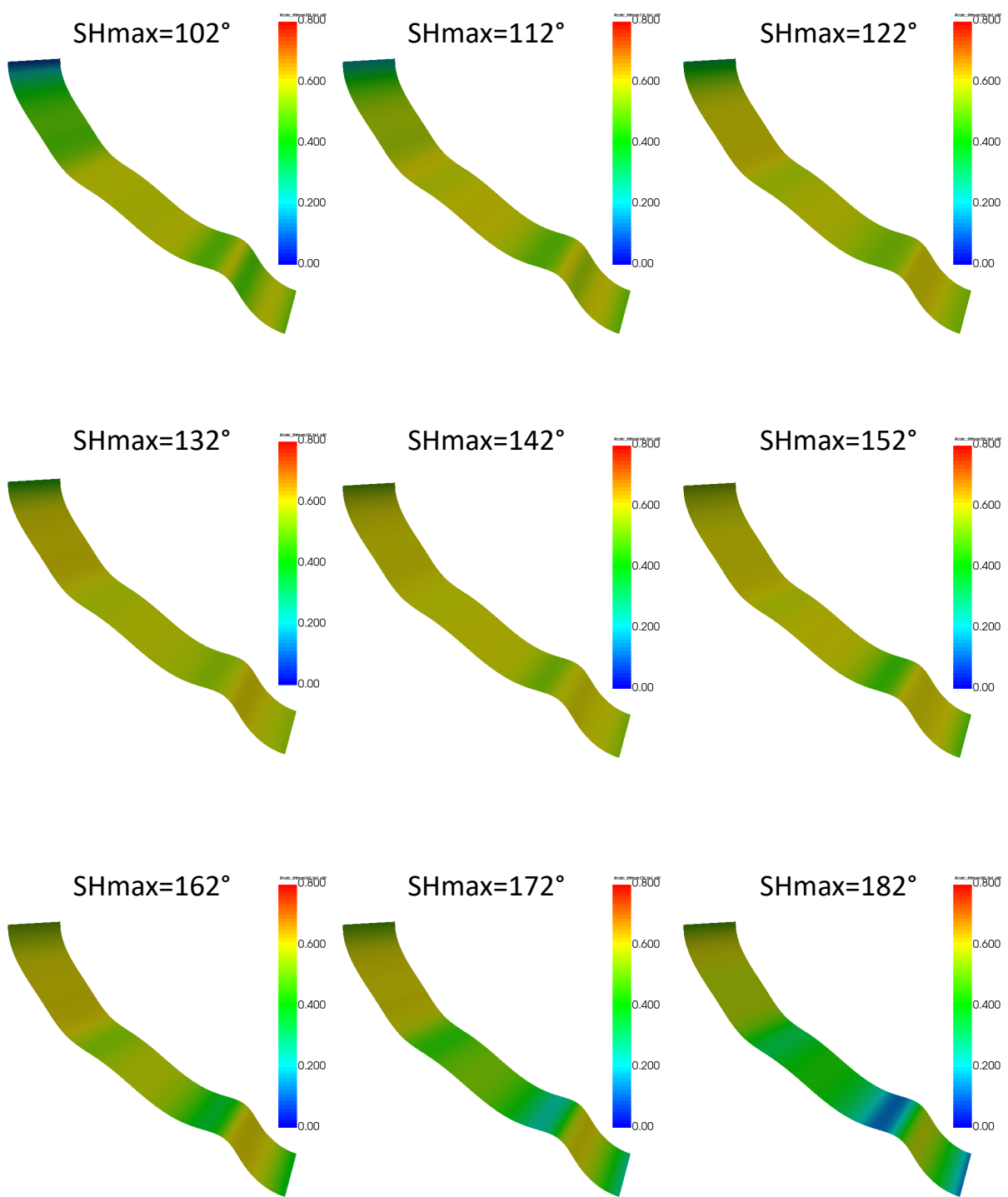


Figure 6: Distribution of relative prestress Ratio  $R$  over the fault. Variation of  $SH_{max}$  from  $102^\circ$  to  $182^\circ$ .

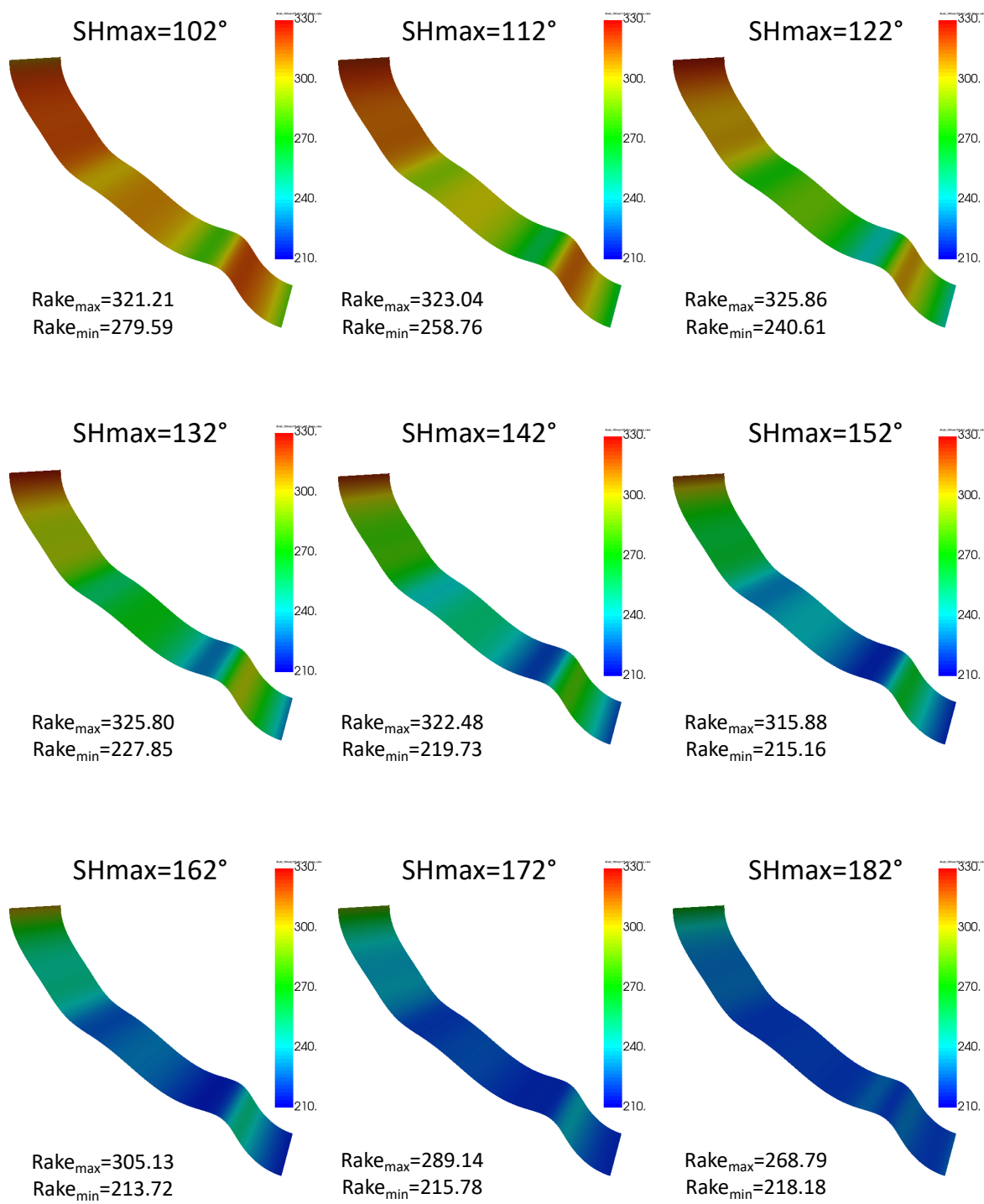


Figure 7: Distribution of the rake angle over the fault. Variation of  $SH_{max}$  from  $102^\circ$  to  $182^\circ$ . Minimum and maximum values for the rake angle are given for each constellation.

# 4 Dynamic rupture modeling

## 4.1 Mesh generation

To run dynamic rupture models we need to discretize the geometry around our fault. We use the meshing software [Simmodeler](#) to generate an [unstructured computational mesh of 1.9 million tetrahedral elements](#). This allows greater geometric flexibility compared to hexahedral element meshes. Since we use a 3D surface wave velocity model, our model does not include geological layers. According to the velocity model, geological properties will be assigned to every cell of the mesh later in dynamic rupture modeling. The fault of the 2017 Botswana earthquake does not intersect the free surface. Therefore, there is no need to integrate topography in our mesh for our purpose.

As computational costs for dynamic rupture modeling depend on the amount of cells, the mesh for our first numerical experiments should be coarse enough. When we have better constrained our simulation parameters, we can apply a higher resolution for our mesh. To limit the amount of cells, we subdivide our model into two sections. The first mesh is big enough to simulate 10 s of wavefield propagation, in order to have a closer look on what happens on the fault after nucleating the earthquake. Here, it is important to avoid reflections of waves back to the fault. If this test reveals an interesting case, the wavefield propagation will be simulated in a bigger mesh to produce synthetic seismogramms with a length of 30 s. Here, we need to avoid reflections of propagated waves back to our region of interest.

### 4.1.1 Mesh dimensions

To define the size of the mesh box around our fault we consider wave propagation velocities. According to the length of our simulation of 10 s and 30 s, the outer edges of the box need to be 87.5 km and 262.5 km off the fault. Here we roughly estimate the fastest P wave velocity to be 8.75 km/s, since we find a [maximum shear wave velocity of 5 km/s](#) in our velocity model and [Fadel et al. \[2018\]](#) suggests a  $v_p/v_s$  ratio of about 1.75 in the region of the Moijabana event. The [minimum shear wave velocity we see in our model is in the area of 2.5 km/s](#).

The spatial discretization of our model determines the resolved frequency of our wavefield. In order to keep the amount of cells smaller than 3 million (to save computing costs) and as the calculation of the mesh resolution is very time-consuming, we follow the approach of Ulrich et al. [\[2019b\]](#) and use an element edge length of [300 m](#) close to the fault, and [10 km over a regional domain](#). This means, we can resolve frequencies up to 4 Hz on the fault (we need 2 elements to resolve the greatest wave length and

the minimum shear wave velocity is  $2.5 \text{ km/s}$ ). The mesh resolution is coarsened away from the fault by using a **gradiation rate of 0.3**. This increases the edge length size of the tetrahedral elements away from the fault. An increasing gradiation rate would lead to decreasing the cell number. The **aspect ratio defines quality levels that the mesher will try to enforce**. We use **aspect ratios** of 6.0 on the fault and 12.0 everywhere else.

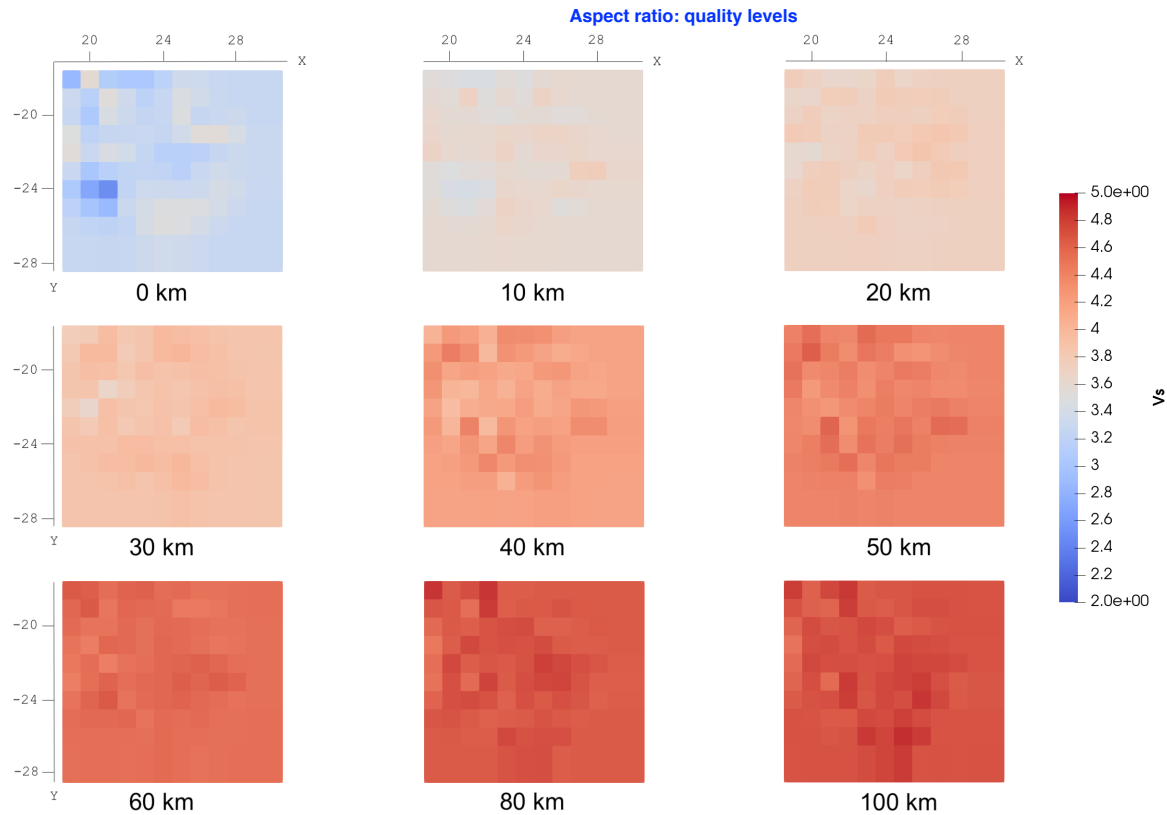


Figure 8: Slices through the shear wave velocity model in given depths.

The low-velocity-anomaly we can see in the plot for the surface wave velocity is apart from any known geological features. **This area is part of the so called Nosop Basin and is characterized by thick sediment cover of more than 7.5 km (see 2)**. Therefore, we consider this anomaly to be related to sediment effects on surface wave velocity attenuation.

#### 4.1.2 Resulting mesh and quality assessment

The **aspect ratio describes the quality of the mesh**. It is to be noted, that the mesher will not strictly create a mesh that passes all the shape metric sets. A simple mesh can reach aspect ratios smaller than 10, complex meshes lead to values up to 40. After the mesh is created, badly shaped elements can be detected by filtering according to aspect ratios. If they are related to geometric features of the model, they should be modified to enable meshes of higher quality. The resulting mesh we use for our first test ("10 s box") consists of 1865341 tetrahedral elements of which 99% show aspect ratios smaller

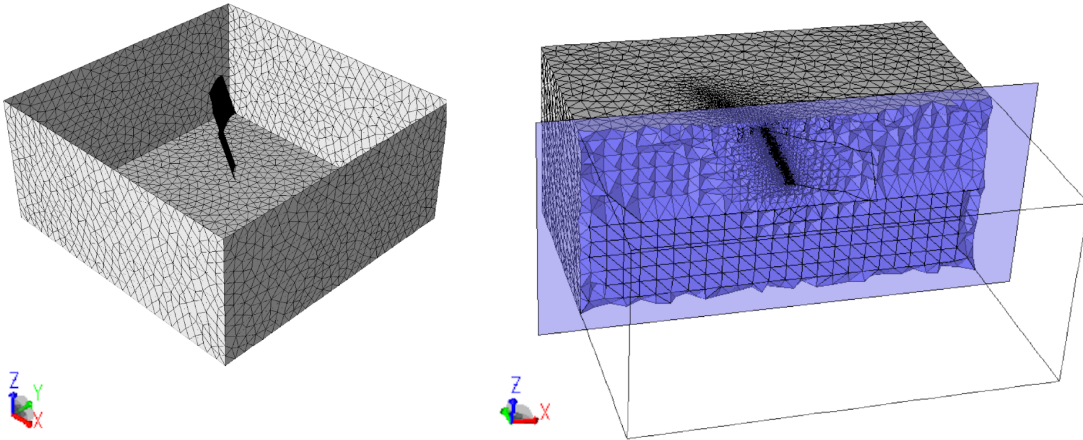


Figure 9: Generated mesh (without surface) on the left. Clipped mesh on the right. Element size changes with the distance to the fault.

[when aspect ratio < 10 is good?](#)

than 10 and no elements with an aspect ratio greater than 20. According to the small spread, we can define our mesh as a simple mesh with good quality throughout.

## 4.2 Dynamic rupture modeling setup

We study the dynamic rupture process under variable regional stress conditions derived from static stress analysis using the open-source and high-performance-computing compatible software package SeisSol (<https://github.com/SeisSol/SeisSol>). By using unstructured tetrahedral meshes, the software combines seismic wave propagation in complex media and frictional fault failure, which enables simulating complex geometric features across a large range of scales [Palgunadi et al., 2020].

Dynamic rupture propagation is primarily determined by fault geometry, material properties, initial stress and nucleation stress conditions, fault strength and a dynamic friction law. Various files are used to implement this information into the model and are shortly introduced in the following. All the input parameters are adapted from the modeling setup used in Palgunadi et al. [2020].

### 4.2.1 Input files

Our mesh describes the fault geometry and the region of study. In order to assign material properties to every cell of the mesh, the 3D velocity model is translated into a material NetCDF file suitable for SeisSol and then provides density  $\rho$  and elastic parameters  $\lambda$  and  $\mu$ .

The fault file contains rate and state friction parameters and reads the initial and nucleation stress files. Since the fault of the Botswana earthquake is buried in depth, it can be strongly simplified compared to the one used in Palgunadi et al. [2020].

The initial stress file describes initial loading conditions, whereas the nucleation stress file only describes the stress conditions at the nucleation area. As we want to make sure that the fault breaks here at first, the prestress ratio  $R$  needs to be higher at the hypocentre. We use a projection perpendicular from the fault to the hypocentre from the USGS catalogue to find the coordinates of our hypocentre, which needs to be on the modeled fault.

All general SeisSol parameters are described in a parameter file which then reads the mesh and the material and fault properties.

### 4.2.2 Rapid weakening friction law

Regional stress conditions were constrained by static analysis investigations. We have described the static strength of the fault and now need to integrate a dynamic component to describe the fault strength. Our initial conditions now are described by background stress regime and in addition, a friction law. To meet this, we use a state of the art and complex friction law with rapid weakening at high slip velocity. This law describes the dramatic friction decrease known from small-scale laboratory experiments at co-seismic slip rates. All underlying equations are described in the method section in Ulrich et al. [2019a]. The friction law mainly depends on the slip rate and a state variable, which empirically describes microscopic processes at contact areas. Fault weakening is proportional to the slip rate  $v$  and according to that, the strength of the fault decreases by a factor of  $1/v$ . The fault friction parameters in table 4.2.1 are similar to those used in Palgunadi et al. [2020] and describe realistic levels of static and dynamic frictional behaviour and stress drop.

Parameter	Symbol	Value
Direct effect parameter	$a$	$0.01 \cdot z$
Evolution effect parameter	$b$	0.014
Reference slip velocity	$V_0$	$10^{-6} \text{ m/s}$
Steady-state friction coefficient at $V_0$	$f_0$	0.6
State-evolution distance	$L$	0.2 m
Weakening slip velocity	$V_W$	$0.1 \cdot z$
Fully weakened friction coefficient	$f_W$	0.1
Initial slip rate	$V_{ini}$	$10^{-16} \text{ m/s}$

Table 4.2.1: Rapid weakening friction law parameters used for dynamic rupture simulations. Note, the direct effect parameter and the weakening slip velocity are depth dependent. The steady state friction coefficient  $f_0$  needs to be similar to the static friction coefficient  $\mu_s$  used in the static analysis.

## 4.3 Results and discussion

The overall objective is to generate synthetic data, to compare it to data published in literature and then to conclude on the quality of our model. If well justified, we can try to give approaches to discuss on the ideas which mechanisms enabled the 2017 Botswana intraplate earthquake. Due to limitations in time for this thesis, we will not be able to conclude on the models of intraplate earthquakes and on the trigger hypothesis for the Botswana earthquake in general. In order to do so, we would need to run a large number of simulations with different setups to constrain all conditions in detail.

Therefore we focus on two sorts of output that can be produced with SeisSol. For one thing we want to discuss the simulated fault outputs like slip distances, slip rates or rupture velocity. In addition to that, we discuss the free surface output, which is comparable with surface deformation out of InSAR measurements.

To conclude on the quality of the model we compute synthetic seismogramms for a comparison with the observed seismogramms from the Mojabana event. Here typical characteristics like first arrival times, delay times between compressional and shear wave arrivals or main seismic energy arrivals are observed. Absolute magnitudes will not be compared due to measurement errors of some seismometers close to the epicentre, which went into saturation and cutted off the maximum amplitude.

Since the 2017 Botswana event is often related to fluid migration we perform two simulations, one under hydrostatic and the other one under lithostatic conditions to probably give some estimations on the role of fluids.

To run dynamic rupture simulations we need to define values for  $SHmax$ ,  $R_0$  and the fluid pressure  $\gamma$ . It is to mention, that these values will not be varied during the simulation, changes in these parameters require a new simulation for each setup. Our results from static analysis recommend to set  $SHmax$  to  $132^\circ$ , since this shows (together with  $SHmax = 142^\circ$ ) the maximum distribution of the R ratio on the fault and the rake angle fits well with normal faulting events. Static analysis results did not provide any findings on  $R_0$  and fluid pressure restrictions. However, we found that  $R_0 = 0.8$  leads to an earthquake that is far to big and therefore defined  $R_0$  to be 0.7 for both simulations. The situation is similar with the fluid pressure. Hydrostatic conditions ( $\gamma = 0.37$ ) lead to great slip distances on the fault, which do not fit with the observations published in literature. Therefore we used lithostatic conditions for the first simulation and set  $\gamma$  to a value of 0.95. The following results all refer to our lithostatic model, since this better describes the overall characteristics. Due to a crash in the simulation and the shutdown of SuperMUC-NG, the results of the simulation under hydrostatic conditions were not yet available at the time the thesis was submitted. Hence, we can only do a quantitative comparison of the lithostatic and hydrostatic simulation results. We expect the simulated earthquake under hydrostatic conditions to be greater than the one under lithostatic conditions. This means slip distances on the fault increase and the computed magnitude is surely greater than  $M6.5$ . Since the fluid pressure  $P_f$  increases with increasing  $\gamma$ , it is not very intuitive, that this decreases the size of the earthquake. However, when we consider the effective confining stress  $\sigma_{eff}$  (equation 3.2.3), it gets clear that an overpressurized state of the fluid pressure ratio  $\gamma$  leads to smaller earthquakes.

### 4.3.1 Free surface output

#### Focal mechanism

To evaluate whether our model appropriately describes the main characteristics of the 2017 Botswana event, we first discuss the calculated moment tensor of our simulation to ensure, that displacement directions fit with real data. The focal mechanism is illustrated through a beachball, which is derived from the solution of the moment tensor for the modeled earthquake and describes the deformation of the source region. The resulting focal mechanism of our model is oblique normal faulting. This coincides with the fault plane solution of other authors, which mainly state normal, or oblique normal faulting [cf. Fadel, Paulssen, et al., 2020, Gardonio et al., 2018, Materna et al., 2019]. Their solutions slightly differ by greater strike angles and smaller dip angles throughout. To describe slip in dip and strike directions quantitatively, we calculated these outputs in our model. This resulted in peak slips of  $-3.5\text{ m}$  in dip direction and  $0.35\text{ m}$  in strike direction. Thus, there is a difference of one order in magnitude between the slip values, which describes a typical normal faulting focal mechanism. Our resulting focal mechanism differs partly from other observations. But compared to the large number of assumptions that have been incorporated into the model and as the main characteristics of compression and dilatation agree with other observations, the computed surface displacement can be properly compared with InSAR displacements.

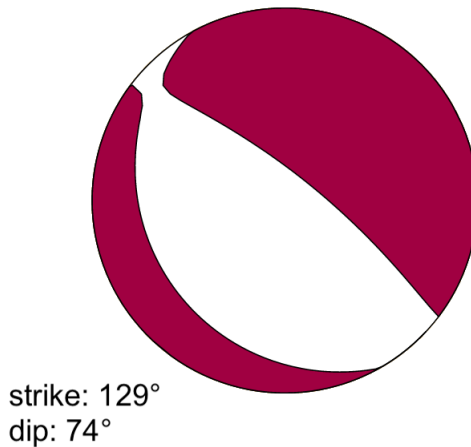


Figure 10: Computed focal mechanism illustrated by a beachball. Red areas correspond to compression, white areas to dilatation.

## Surface displacement

Our fault is placed in 5 km depth and is not connected to any topographic features. However, we can compute a free surface output on the top of our model domain. From the resulting displacements in three dimensions, we obtain horizontal and vertical displacement. Materna et al. [2019] computed displacements based on InSAR measurements. Unfortunately, there is no information on the line of sight (LOS) configuration they used and therefore we can not use our displacements to generate a corresponding plot to better compare the findings. But vertical and horizontal displacement together result in absolute displacement, which is similar to InSAR displacement and can be compared at least.

Our results for the horizontal displacement show greater displacements on the north-eastern side of the fault. Here,  $-2.5\text{ cm}$  of displacement occurred, whereas on the south-western side smaller displacements of  $-2\text{ cm}$  result from the simulation. There are parts with positive displacements spreading circular from the fault. This is due to the propagating wavefront and has no physical meaning. We did not plot the displacement at the end of the simulation since reflections from absorbing boundaries would rework our region of interest. Vertical displacements behave different to the horizontal displacements. Since the Mojabana event and our model show a normal faulting focal mechanism (see figure 10), we expect displacement on the north-eastern side to be negative and positive on the opposite side of the fault. This is consistent with the peak displacements of  $-4.0\text{ cm}$  on the north-eastern side and  $2.5\text{ cm}$  on the south-western side.

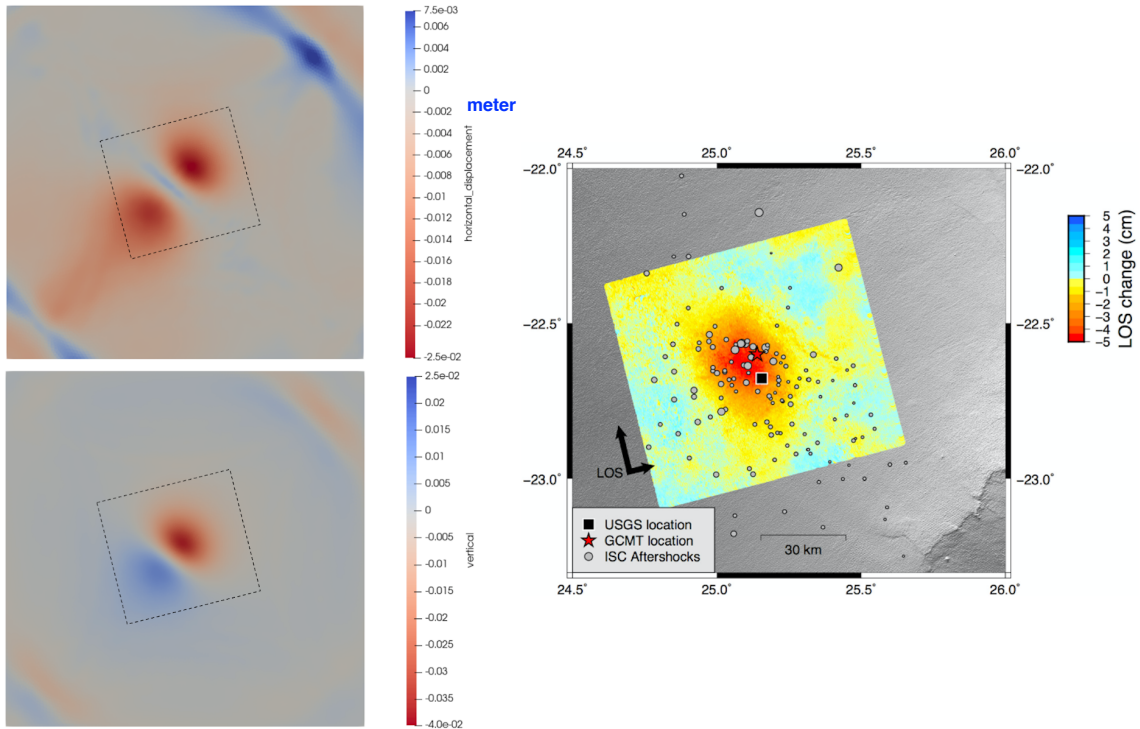


Figure 11: Horizontal and vertical displacements of our lithostatic model. Dashed rectangle marks the area corresponding to the data from Materna et al., 2019. Figure on the right: InSAR displacements from Materna et al.

The findings from Materna et al. show maximum LOS displacements of  $-5\text{ cm}$ . When we combine our horizontal and vertical displacements, we obtain displacements with similar magnitudes. The location of the hypocentre is based on the location from the USGS catalogue, which is also marked in the InSAR plot from Materna et al. When we now compare the spatial distribution of InSAR displacement around the earthquake location with our observations, it seems like our results show similar displacement distributions, but rotated anticlockwise to the earthquake location. This feature can also be seen when we compare our moment tensor solution (where we obtain a smaller strike angle, see figure 10) with the data published. A smaller strike angle can be graphically interpreted as a rotation around the epicentre in the case of displacement.

## Synthetic seismograms

To further quantify the quality of our results regarding wave propagation off the fault we use synthetic seismograms. There are some seismometers placed in the vicinity of the 2017 Botswana earthquake which we want to use for a comparison with computed seismograms at the same location. We are limited in the number of stations due to the dimension of our model domain. However, there are two stations from the seismographic network of IRIS in the region of interest. To be comparable, both seismographic data sets need to contain the same range of frequencies. Here we used the conservative estimation of taking two wavelengths per element to find our resolved frequency over the domain. Our element size over regional scale is  $10\text{ km}$  and the average shear wave velocity is approximately  $3.3\text{ km/s}$ , which leads to a resolved frequency of about  $0.6\text{ Hz}$ . Thus, determined by our model setup, we applied a butterworth bandpass filter to the real data with lower and upper boundaries of  $0.2\text{ Hz}$  and  $0.6\text{ Hz}$ , respectively. Note, a prefilter was applied to the raw data set in order to avoid noise from instrument responses at the beginning of the seismogramm. All seismic data was taken from <https://ds.iris.edu/ds/nodes/dmc/data> (we use  $20\text{ Hz}$  broadband seismometer data set). It is to be noted, that due to reflections at absorbing boundaries of the model domain, signal pollution has to be expected after  $30\text{ s}$  at the least. This is why the plotted data is without relevance for us after this point.

Although we only have little data to compare, there are some interesting features worth to be discussed.

First we want to focus on station NE212, which corresponds to receiver number 3 in our model. Here, we can clearly see that first arrivals of p-waves fit with the real data in time and polarity. Unfortunately, after two wave periods, real and synthetic data do not coincide until it gets accurate once more after approximately  $25\text{ s}$  of simulation time. The distance between the earthquake and Station NE212 is about  $89\text{ km}$  and our velocity model show shear wave velocities of  $3.1$  to  $3.6\text{ km/s}$  in shallow depths. Therefore, the second correspondance of the phases probably shows the arrival of secondary waves.

If we take a look at the data of station NE208, the computed seismographic data does not really reproduce first arrival times of primary waves. However, we can see that the arrival of shear waves, at least for the first and the second component, can be detected. In contrast to the left seismogramm, phase amplitudes do not match with the real data in this case. There are two negative spikes at approximatley  $25\text{ s}$  in the northern and

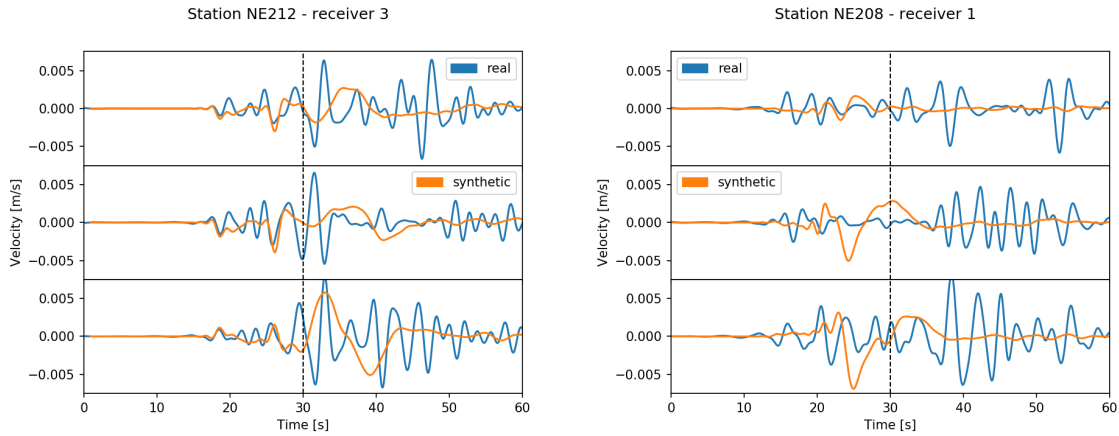


Figure 12: Comparison of real and synthetic seismogramms for all three components (east, north, vertical). Due to reflections from absorbing boundaries of our model domain, data right to the dashed line is not representative for the model.

vertical component, which probably show interfering reflected waves, as they do not fit with any characteristics of the real data.

Overall, the computed data for station NE212 shows higher coincidence with the real data and although we have made strong simplifications in our model setup, we can reproduce some characteristic features. This shows, that our velocity model, which was translated into 3D material properties, and the parametrization of the source represent realistic conditions, but need to be specified in large parts.

### 4.3.2 Fault output

#### Absolute slip on the fault

After we found some consistencies in real and simulated data regarding the surface of our model domain, we now take a closer look at what is happening directly on the fault. Our model produces a peak slip of  $3.6\text{ m}$  at the nucleation center and an average slip of  $\approx 0.7\text{ m}$ . The magnitude of our simulated earthquake is  $M6.46$ , which is consistent with all other observations on the 2017 Botswana earthquake. In figure 13 b), we see the right and left end of the rupture propagation coinciding with changes in the fault's curvature. Here, geometric barriers result in greater dynamic fault strength, which stress, accumulated due to the rupture, can not overcome. In terms of our 3D discretization this means, that optimal and non-optimal oriented tetrahedral elements act in a way forcing the rupture to stop there. When we designed our model, we estimated the end of the seismogenic zone to be in  $37\text{ km}$  depth, that's why rupture propagation stops here horizontally. The model setup also included a depth-dependent stress tensor, which determines the end of the slip propagation upwards in vertical direction. We find that rupture stops very smoothly at a depth of  $17\text{ km}$  in the middle of our fault plane. This is a sign for a fragile dynamic balance of our model. This means that rupture can be stopped easily on the fault, but far more important, that we found a

state of stress, which describes conditions very close to failure equilibrium. So close that geometric barriers stop the rupture propagating. These findings coincide with our results from the static analysis (6). The distribution of relative prestress ratio  $R$  strongly depends on the curvature of our fault plane and reaches peak values in the hypocentral area. Since  $R$  describes how close a point on the fault is to failure, the slip distribution fits with the findings on distributions of  $R$  ratios. This suggests that the 2017 Botswana event happened in an area where local stress accumulation reached a level where a moderate trigger action lead to failure.

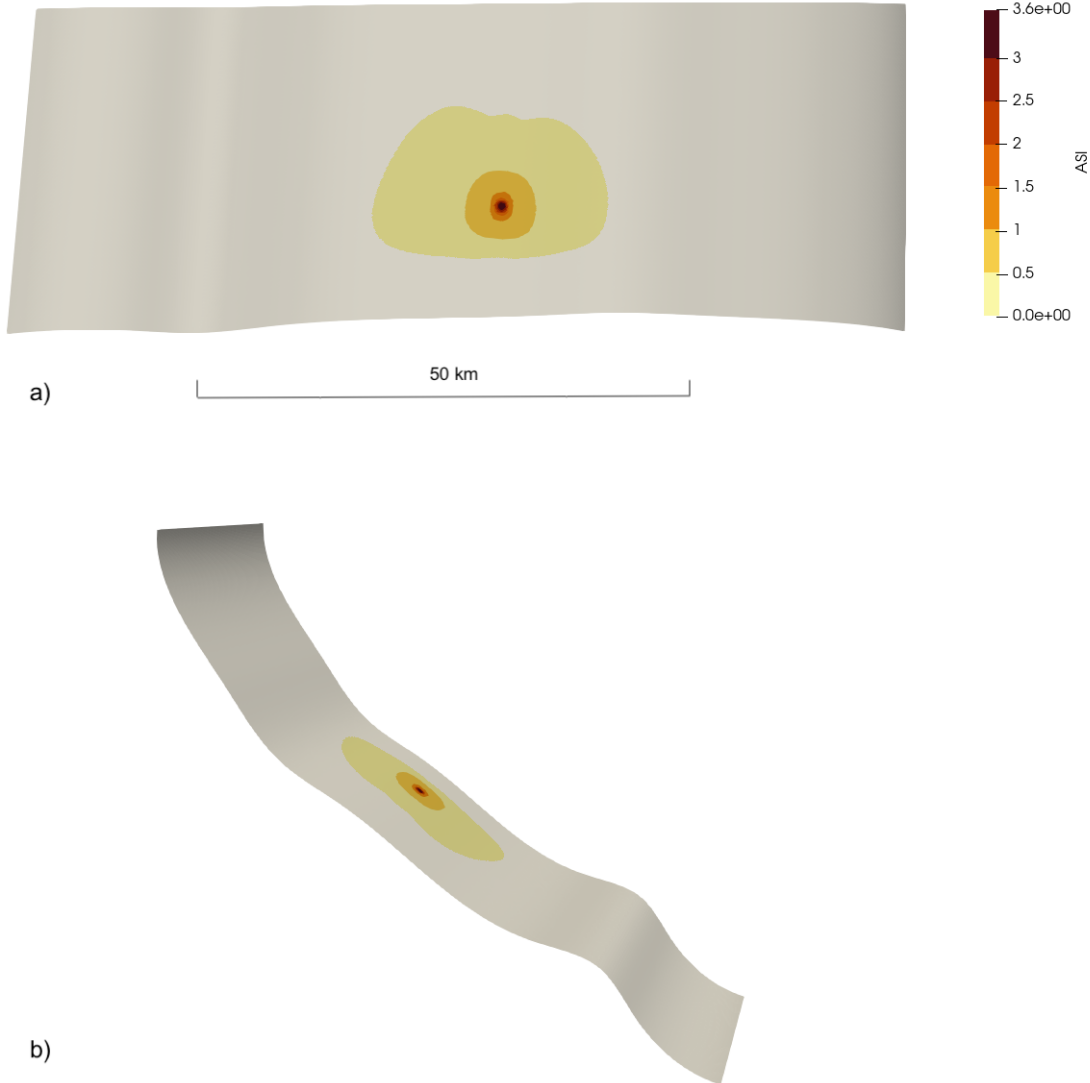


Figure 13: a) Absolute slip on the fault in  $m$ . b) Geometric barriers stop rupture propagation.

In general, our fault patch is the size of  $23 \times 14 \text{ km}$  and after  $6 \text{ s}$ , rupture stopped on the fault. Materna et al. [2019] suggest a rupture duration of  $10 \text{ s}$ , splitted into two asperities. Since the duration of our rupture is limited due to geometric barriers, that are not part of the model from Materna et al., both values describe relatively similar scenarios. Interestingly, Materna et al. used a slip patch, that is almost equal to our

observed slip patch in size and geometry ( $23.4 \times 13.6 \text{ km}$ ). Hence, it is not surprising that the slip value of  $0.66 \text{ m}$  describing their source is also consistent with the average slip of our model ( $\approx 0.7 \text{ m}$ ). On the other side, Materna et al. suggest a maximum slip of  $0.8 \text{ m}$ , whereas our model shows a peak of greater than  $3 \text{ m}$ . This may be due to the simple source parametrization we made. Here, a more detailed description of the nucleation might bring some improvements for our slip distribution on the fault. However, we need to remember that the fault trace is based on estimations according to a resistivity model by Max Moorkamp. Therefore, uncertainties regarding the fault trace and, accordingly, also regarding the shape and location of geometric barriers must be considered. It is also possible, that the estimated geometric barriers are in fact rather geologic barriers resulting from heterogeneities in rock compositions. Here, we can not clearly distinguish between these two options, but we can be fairly confident, that the resistivity model of Max Moorkamp adequately sustains the geometric barrier hypothesis. As the fault is buried in depth, detailed measurements of structural and geological features would be necessary to clearly identify the real fault trace.

## Slip rates

By carrying out dynamic simulations, we are not only interested in the result after the simulation has stopped. Valuable insights can be gained by studying spatial and temporal development of the rupture, especially from the rate of the development.

Slip rates describe velocities of particles on the fault in strike and dip direction. We observe relatively small slip rates in strike direction ( $0.56 \text{ m/s}$ ) compared to the slip rates in dip direction ( $-2.4 \text{ m/s}$ ). The slip rate shows how the rupture propagates in time and space on our fault and shows i.e. the location, at which time of simulation the fault breaks. Since slip rates immediately go back to zero after the rupture, we can describe our modeled rupture as a pulse-like event. This can be detected due to rate-and-state friction approach in dynamic rupture modeling. In general, high slip rates indicate high ground motion and vice versa. We observed a peak slip rate of  $2.4 \text{ m/s}$ , which is not unusually big for a  $M6.5$  event. A macroseismic survey from Midzi et al. [2018] shows intensities of  $V\text{-}VI$  in the epicentral area, which corresponds to noticeable ground shaking effects, but does not produce significant damages. Since the epicentral region is covered by thick sand deposits and nearly no damage occurred, slip rates of the Mojabana event could have been higher than indicated by the observed damages. However, it is likely that slip rates of the Mojabana earthquake have not been very high and our model produces realistic values. Another interesting feature of our simulation is that the rupture propagates bilaterally. This means, that the rupture stops earlier in SE direction than in NW direction, which is due to geometric complexities where stresses are too low to sustain rupture.

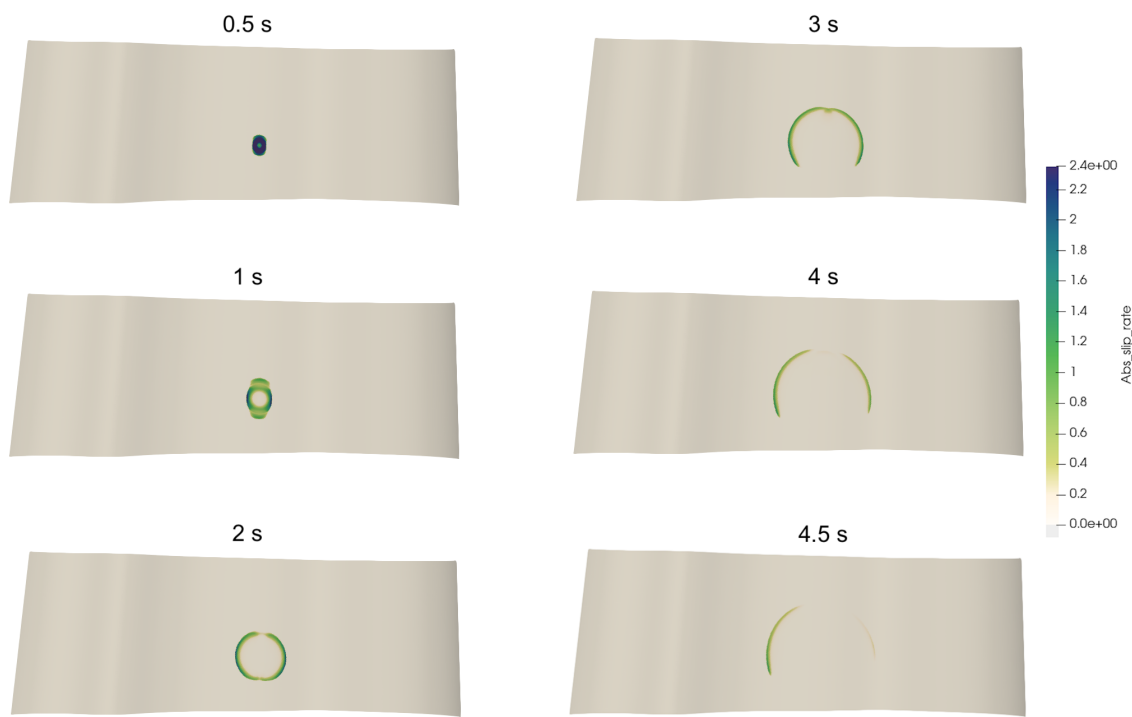


Figure 14: Space and time evolution of the slip rate on the fault (in  $m/s$ ).

# 5 Conclusion and outlook

In this thesis we studied static stress conditions to derive a realistic state of stress which enables an intraplate earthquake like the 2017 Botswana event. Based on these findings, we designed a kinematic model with an integrated 3D surface wave model to carry out dynamic rupture simulations. Our model setup for the lithostatic state of pressure shows several characteristics matching with observations published in literature and is in general a good approximation to real conditions in the Moijabana region. However, our hydrostatic model describes an earthquake much greater than the *M*6.5 event in Botswana. This does not necessarily mean that the Moijabana earthquake definitely happened under lithostatic conditions. It is rather an indicator, that under the conditions we chose for our model, hydrostatic conditions do not fit, whereas they can fit under different conditions.

To push the project ahead, we need to quantitatively review the assumptions we made an inputs we used during this thesis.

We started by modeling a fault based on a resistivity distribution by Max Moorkamp. Dip and strike values have been used from observations published in literature and therefore contain uncertainties, which combined with the estimated and smoothed fault trace (to avoid problems in numerical modeling), end up in a very rough estimation on the real location and geometry of the Moijabana fault. Even if it agrees well with the observed aftershock distribution (see figure 5), the fault may consists of some listric parts and characteristic curvatures may differ to the real fault geometry. This can directly affect prestress ratios and rupture propagation on the fault.

Rupture propagation also depends on the location of the hypocenter, which we estimated by projecting the location of the USGS catalogue perpendicular onto our fault. It is obvious that this leads to first order uncertainties. To better distinguish about the hypocentre location, one could use the location of the aftershocks (as they correlate with the 'boundary' where slip of a mainshock stops) and the waveforms with a velocity model to find the point on the fault, that could generate the most coherent signal. The geometry of our fault therefore can be improved in some parts, but according to given data, we found a good estimation of the fault geometrics.

Our dynamic model required a 3D discretization of our model domain. The resulting mesh is coarsened away from the fault and is not designed to resolve small-scale details over the model domain. In general, one might think higher resolution leads to higher quality of the results, but since geological data for the Moijabana region is rare and varies in quality, it can not be assumed to gain better simulation results by only increasing the mesh resolution. In this context, it is worth to evaluate the impact of the shear wave velocity model on our results. The quality of the model in the region of interest is good, but since we only have information on shear wave velocities, compressional wave velocities have been estimated by a  $v_p/v_s$  ratio from Fadel et al. [2018] and calculated material properties therefore contain uncertainties which are difficult to clar-

ify. But compared to general uncertainties, our material properties are well understood compared to other parameters.

Our simulations required a variety of parameters which mostly have been derived from Palgunadi et al. [2020]. These values describe realistic conditions and are sufficient to run the first dynamic simulations. However, they were specifically calculated for the project of Palgunadi et al. and therefore may have been slightly different, if they had been calculated individually for the Botswana project. It is difficult to estimate the possible improvements in this case, especially when we consider the time consuming procedure of calculating the parameters individually, but there certainly is potential for improvements. For example, our initial stress conditions have been observed by static stress analysis. The nucleation stress conditions however, have been taken from Palgunadi et al. and can be specified for the case of the Botswana event as well.

Based on the results of this thesis, several actions need to be carried out to improve the quality of our results, to better parameterize our model and to conclude on trigger mechanisms and intraplate seismicity in general. We have simulated two cases, a lithostatic and a hydrostatic case. It is obvious, that more simulations with different stress conditions regarding stress directions and magnitudes will provide a more reliable data basis. Different scenarios of static analysis results can be simulated in the dynamic case to quantitatively estimate the excess of change for different stress conditions. These results can be used to discuss the models on intraplate seismicity as well as for refining our model.

In order to improve our model in general, the next step is to design a much larger model domain. Reflections from absorbing boundaries polluted our simulation results and made them useless in parts. To avoid these problems, a larger mesh is required. Especially waveform comparisons would be more reliable and could provide some valuable results to estimate the accuracy of our model. In this context, a larger model domain additionally enables us to use more stations in the region of Mojabana, which then consolidates the seismographic results.

Another important step is to discuss the results of the simulation under hydrostatic conditions in detail. It is necessary to quantify the differences between two setups with similar parametrization except the state of pressure to gain an understanding, whether the role of basement pressurization is that important that we now think it is. Maybe the differences in the prestress ratio  $R_0$  play a much more important role on the size of the earthquake and the state of pressure is only contributing to a lower extent.

When all these improvements are carried out, we will definitely have a better understanding on the general role of the main parameters and can design a set of models which will describe the Mojabana event very accurate. Based on this, estimations on the mechanisms of intraplate earthquakes can be made.

# Bibliography

- Adams, Aubreya and Andrew Nyblade (June 2011). “Shear wave velocity structure of the Southern African upper mantle with implications for the uplift of Southern Africa”. In: *Geophysical Journal International* 186, pp. 808–824.
- Albano, Matteo, Marco Polcari, Christian Bignami, Marco Moro, Michele Saroli, and Salvatore Stramondo (Oct. 2017). “Did Anthropogenic Activities Trigger the 3 April 2017 Mw 6.5 Botswana Earthquake?” In: *Remote Sensing* 9.
- Aochi, Hideo and Raúl Madariaga (June 2003). “The 1999 Izmit, Turkey, Earthquake: Nonplanar Fault Structure, Dynamic Rupture Process, and Strong Ground Motion”. In: *Bulletin of the Seismological Society of America* 93.3, pp. 1249–1266.
- Barbee, Jeffrey (Apr. 2017). *Did fracking in Botswana cause Johannesburg to tremble?* Website: <https://www.dailymaverick.co.za/article/2017-04-04-did-fracking-in-botswana-cause-johannesburg-to-tremble/>.
- Begg, Graham et al. (Feb. 2009). “The lithospheric architecture of Africa: Seismic tomography, mantle petrology, and tectonic evolution”. In: *Geosphere* 5, pp. 23–50.
- Bowman, J. R. (1992). “The 1988 Tennant Creek, northern territory, earthquakes: A synthesis”. In: *Australian Journal of Earth Sciences* 39.5, pp. 651–669.
- Bufford, Kelsey et al. (Apr. 2012). “Geometry and faults tectonic activity of the Okavango Rift Zone, Botswana: Evidence from magnetotelluric and electrical resistivity tomography imaging”. In: *Journal of African Earth Sciences* 65, pp. 61–71.
- Byerlee, J. (1978). “Friction of rocks”. In: *pure and applied geophysics* 116.4, pp. 615–626.
- Calais, E., T. Camelbeeck, S. Stein, M. Liu, and T. J. Craig (2016). “A new paradigm for large earthquakes in stable continental plate interiors”. In: *Geophysical Research Letters* 43.20, pp. 10, 621–10, 637.
- Clark, Dan, Andrew McPherson, and Russ [Van Dissen] (2012). “Long-term behaviour of Australian stable continental region (SCR) faults”. In: *Tectonophysics* 566–567, pp. 1–30.
- Clauser, Christoph (2016). *Einführung in die Geophysik*. 2nd ed. Springer Spektrum.

- Craig, T. J., J. A. Jackson, K. Priestley, and D. McKenzie (2011). “Earthquake distribution patterns in Africa: their relationship to variations in lithospheric and geological structure, and their rheological implications”. In: *Geophysical Journal International* 185.1, pp. 403–434.
- Demets, C., Richard Gordon, and Donald Argus (Apr. 2010). “Geological current plate motions”. In: *Geophysical Journal International - GEOPHYS J INT* 181, pp. 1–80.
- Fadel, Islam, Mark van der Meijde, and Hanneke Paulssen (2018). “Crustal Structure and Dynamics of Botswana”. In: *Journal of Geophysical Research: Solid Earth* 123.12, pp. 10, 659–10, 671.
- Fadel, Islam, Hanneke Paulssen, Mark van der Meijde, Motsamai Kwadiba, Onkgopotse Ntibinyane, Andrew Nyblade, and Raymond Durrheim (2020). “Crustal and Upper Mantle Shear Wave Velocity Structure of Botswana: The 3 April 2017 Central Botswana Earthquake Linked to the East African Rift System”. In: *Geophysical Research Letters* 47.4.
- Gardonio, B., R. Jolivet, E. Calais, and H. Leclère (2018). “The April 2017 Mw6.5 Botswana Earthquake: An Intraplate Event Triggered by Deep Fluids”. In: *Geophysical Research Letters* 45.17, pp. 8886–8896.
- Heidbach, Oliver, Mojtaba Rajabi, Karsten Reiter, Moritz Ziegler, and WSM Team (2016). “World Stress Map Database Release 2016”. In: *Website*.
- Hough, Susan E., John G. Armbruster, Leonardo Seeber, and Jerry F. Hough (2000). “On the Modified Mercalli intensities and magnitudes of the 1811–1812 New Madrid earthquakes”. In: *Journal of Geophysical Research: Solid Earth* 105.B10, pp. 23839–23864.
- Hutchins, D. G. and Botswana. Geological Survey Department (1976). *A Summary of the geology, seismicity, geomorphology, and hydrogeology of the Okavango Delta / by D.G. Hutchins ... [et al.]* Botswana. Geological Survey Department Bulletin - Geological Survey Department, Republic of Botswana ; 7. Lobastse, Botswana: Geological Survey Dept.
- Jacobs, Joachim, Sergei Pisarevsky, Bob Thomas, and Thomas Fullgraf (Jan. 2008). “The Kalahari Craton during the assembly and dispersal of Rodinia”. In: *Precambrian Research* 160, pp. 142–158.
- James, David, Fenglin Niu, and Juliana Rokosky (Dec. 2003). “Crustal structure of the Kaapvaal Craton and its significance for early crustal evolution”. In: *Lithos* 71, pp. 413–429.
- Kanamori, Hiroo and Emily E Brodsky (July 2004). “The physics of earthquakes”. In: *Reports on Progress in Physics* 67.8, pp. 1429–1496.
- Khoza, T. D., A. G. Jones, M. R. Muller, R. L. Evans, M. P. Miensopust, and S. J. Webb (2013). “Lithospheric structure of an Archean craton and adjacent mobile belt

- revealed from 2-D and 3-D inversion of magnetotelluric data: Example from southern Congo craton in northern Namibia". In: *Journal of Geophysical Research: Solid Earth* 118.8, pp. 4378–4397.
- Kinabo, B.D., Estella Atekwana, John Hogan, Motsoptse Modisi, D.D. Wheaton, and A.B. Kampunzu (June 2007). "Early structural development of the Okavango rift zone, NW Botswana". In: *Journal of African Earth Sciences* 48, pp. 125–136.
- Kolawole, F., E. A. Atekwana, S. Malloy, D. S. Stamps, R. Grandin, M. G. Abdelsalam, K. Leseane, and E. M. Shemang (2017). "Aeromagnetic, gravity, and Differential Interferometric Synthetic Aperture Radar analyses reveal the causative fault of the 3 April 2017 Mw 6.5 Moiyabana, Botswana, earthquake". In: *Geophysical Research Letters* 44.17, pp. 8837–8846.
- Krueger, Frank and Frank Scherbaum (Jan. 2014). "The 29 September 1969, Ceres, South Africa, Earthquake: Full Waveform Moment Tensor Inversion for Point Source and Kinematic Source Parameters". In: *Bulletin of the Seismological Society of America* 104.
- Leseane, Khumo, Estella A. Atekwana, Kevin L. Mickus, Mohamed G. Abdelsalam, Elisha M. Shemang, and Eliot A. Atekwana (2015). "Thermal perturbations beneath the incipient Okavango Rift Zone, northwest Botswana". In: *Journal of Geophysical Research: Solid Earth* 120.2, pp. 1210–1228.
- Liu, Lanbo and Mark Zoback (Aug. 1997). "Lithosphere strength and intraplate seismicity in the New Madrid seismic zone". In: *Tectonics* 16, pp. 585–595.
- Liu, Mian and Seth Stein (Nov. 2016). "Mid-continental earthquakes: Spatiotemporal occurrences, causes, and hazards". English (US). In: *Earth-Science Reviews* 162, pp. 364–386.
- Liu, Mian, Seth Stein, and Hui Wang (Apr. 2011). "2000 years of migrating earthquakes in North China: How earthquakes in midcontinents differ from those at plate boundaries". In: *Lithosphere* 3.2, pp. 128–132.
- Materna, Kathryn, Shengji Wei, Xin Wang, Luo Heng, Teng Wang, Weiwen Chen, Rino Salman, and Roland Burgmann (Jan. 2019). "Source characteristics of the 2017 Mw6.4 Moijabana, Botswana earthquake, a rare lower-crustal event within an ancient zone of weakness". In: *Earth and Planetary Science Letters* 506, pp. 348–359.
- McNamara, D. E., H. M. Benz, R. B. Herrmann, E. A. Bergman, P. Earle, A. Holland, R. Baldwin, and A. Gassner (2015). "Earthquake hypocenters and focal mechanisms in central Oklahoma reveal a complex system of reactivated subsurface strike-slip faulting". In: *Geophysical Research Letters* 42.8, pp. 2742–2749.
- Midzi, Vunganai et al. (Mar. 2018). "The 03 April 2017 Botswana M6.5 Earthquake: Preliminary Results". In: *Journal of African Earth Sciences* 143.

- Modisi, Motsoptse, Estella Atekwana, A. Kampunzu, and T. Ngwisanzi (Oct. 2000). “Rift kinematics during the incipient stages of continental extension: Evidence from the nascent Okavango rift basin, northwest Botswana”. In: *Geology* 28.
- Mooney, Walter, Jeroen Ritsema, and Yong Keun Hwang (Dec. 2012). “Crustal seismicity and the earthquake catalog maximum moment magnitude (Mcmax) in stable continental regions (SCRs): Correlation with the seismic velocity of the lithosphere”. In: *Earth and Planetary Science Letters* 357-358, pp. 78–83.
- Moorkamp, Max, Stewart Fishwick, Richard J. Walker, and Alan G. Jones (2019). “Geophysical evidence for crustal and mantle weak zones controlling intra-plate seismicity – the 2017 Botswana earthquake sequence”. In: *Earth and Planetary Science Letters* 506, pp. 175–183.
- Mosley, K. S. (May 2010). “Geophysical characterization of faults of the Okavango Rift Zone, Northwest Botswana, Africa”. MA thesis. Oklahoma state Univ.
- Palgunadi, Kadek Hendrawan, Alice-Agnes Gabriel, Thomas Ulrich, José Ángel Lopéz-Comino, and Paul Martin Mai (2020). *Dynamic fault interaction during a fluid-injection induced earthquake: The 2017 Mw 5.5 Pohang event*.
- Pastier, Anne-Morwenn, Olivier Dauteuil, Mike Murray-Hudson, Frédérique Moreau, Andrea Walpersdorf, and Kaelo Makati (June 2017). “Is the Okavango Delta the terminus of the East African Rift System? Towards a new geodynamic model: Geodetic study and geophysical review”. In: *Tectonophysics* 712.
- Pollitz, F. F., L. Kellogg, and R. Burgmann (2001). “Sinking mafic body in a reactivated lower crust: A mechanism for stress concentration at the New Madrid seismic zone”. In: *Bulletin of the Seismological Society of America* 91.6, pp. 1882–1897.
- Pretorius, D.A. (1984). *The Kalahari Foreland, its marginal troughs and overthrust belts, and the regional structure of Botswana*. Information circular Nr. 169-172. University of the Witwatersrand.
- Priestley, Keith, Dan McKenzie, and Eric Debayle (2006). “The state of the upper mantle beneath southern Africa”. In: *Tectonophysics* 416.1. The Heterogeneous Mantle, pp. 101–112.
- Reeves, C.V. (1978). “Reconnaissance Aeromagnetic Survey of Botswana, 1975-1977”. In: Final Interpretation Report, Special Publication of the Botswana Geological Survey and the Canadian International Development Agency, 199 pp + appendices.
- Schijndel, Valby, David Cornell, Dirk Frei, Siri Simonsen, and Martin Whitehouse (Jan. 2014). “Crustal evolution of the Rehoboth Province from Archaean to Mesoproterozoic times: Insights from the Rehoboth Basement Inlier”. In: *Precambrian Research* 240, pp. 22–36.
- Shearer, Peter M. (2009). *Introduction to Seismology*. 2nd ed. Cambridge University Press.

- Stamps, D. Sarah, L. Flesch, and Eric Calais (Oct. 2010). “Lithospheric buoyancy forces in Africa from a thin sheet approach”. In: *International Journal of Earth Sciences* 99, pp. 1525–1533.
- Sykes, L. and M. Sbar (1973). “Intraplate Earthquakes, Lithospheric Stresses and the Driving Mechanism of Plate Tectonics”. In: *Nature* 245.5424, pp. 298–302.
- Sykes, Lynn R. (Nov. 1978). “Intraplate seismicity, reactivation of preexisting zones of weakness, alkaline magmatism, and other tectonism postdating continental fragmentation”. In: *Rev. Geophys.* 16.4, pp. 621–688.
- Talwani, P. (Oct. 1988). “The Intersection Model for Intraplate Earthquakes”. In: *Seismological Research Letters* 59.4, pp. 305–310.
- Talwani, Pradeep (2017). “On the nature of intraplate earthquakes”. In: *Journal of Seismology* 21.1, pp. 47–68.
- Ulrich, T. et al. (2019b). “Coupled, Physics-Based Modeling Reveals Earthquake Displacements are Critical to the 2018 Palu, Sulawesi Tsunami”. eng. In: *Pure and Applied Geophysics* 176, pp. 4069–4109.
- Ulrich, Thomas, Alice-Agnes Gabriel, Jean-Paul Ampuero, and Wenbin Xu (2019a).  
“Dynamic viability of the 2016 Mw 7.8 Kaikōura earthquake cascade on weak crustal faults”. In: *Nature Communications* 10.1, p. 1213.
- Wright, C, E.M Kgaswane, M.T.O Kwadiba, R.E Simon, T.K Nguuri, and R McRae-Samuel (2003). “South African seismicity, April 1997 to April 1999, and regional variations in the crust and uppermost mantle of the Kaapvaal craton”. In: *Lithos* 71.2. A Tale of Two Cratons: The Slave-Kaapvaal Workshop, pp. 369–392.
- Yu, Youqiang, Stephen Gao, Moikwathai Moidaki, Cory Reed, and Kelly Liu (Aug. 2015). “Seismic anisotropy beneath the incipient Okavango rift: Implications for rifting initiation”. In: *Earth and Planetary Science Letters* 430.
- Yu, Youqiang, Kelly H. Liu, Cory A. Reed, Moikwathai Moidaki, Kevin Mickus, Estella A. Atekwana, and Stephen S. Gao (2015). “A joint receiver function and gravity study of crustal structure beneath the incipient Okavango Rift, Botswana”. In: *Geophysical Research Letters* 42.20, pp. 8398–8405.
- Zoback, Mary Lou (July 1992). “First- and second-order patterns of stress in the lithosphere: The World Stress Map Project”. In: *J. Geophys. Res.* 97.B8, pp. 11703–11728.

# Acknowledgement

Foremost, I would like to express my sincere gratitude to my supervisors Alice and Max for the support, ideas, data and guidance during my first thesis. Since communicating and working together was different in COVID19 times, I really appreciate that both of you always had time for my questions and a weekly meeting. Thank you for giving me the chance to work on this thesis, where I was part of the whole project cycle from a geophysical model over modelling approaches to our own dynamic rupture simulation. During the last 5 months, I got some deep and valuable insights on how science works and gained a better understanding of seismological research.

Furthermore, I want to express special thanks to Thomas Ulrich, the master of scripts, who always helped me out when I was trapped in some python code and in general, the whole earthquake source physics group of Alice for giving their estimations on my work.

A special thank goes to Jens Oeser and Marcus Mohr for the super fast and uncomplicated help in setting up a vnc-connection to run software remoteley and helping me out in any technical problem related to the IT-infrastructure.

# Statement of authorship

With this statement, I certify that this thesis has been composed by myself. Unless otherwise acknowledged in the text, it describes my own work. All references have been quoted and all sources of information have been specifically acknowledged. This thesis has not been accepted in any previous applications for a degree.

Hiermit versichere ich, dass ich die vorliegende Arbeit selbstständig verfasst und keine anderen als die angegebenen Quellen und Hilfsmittel benutzt habe, alle Ausführungen, die anderen Schriften wörtlich oder sinngemäß entnommen wurden, kenntlich gemacht sind und die Arbeit in gleicher oder ähnlicher Fassung noch nicht Bestandteil einer Studien- oder Prüfungsleistung war.

---

Place, Date

---

Signature